Sánchez-Quesada *et al.*
Advances in Bridge Engineering (2026) 7:28
https://doi.org/10.1186/s43251-026-00217-4

Advances in
Bridge Engineering

ORIGINAL INNOVATION

Open Access

Maximum vertical acceleration patterns in skewed multi-span railway bridges under increasing operational speeds

J. C. Sánchez-Quesada[1], E. Moliner[1*], P. Galvín[2,3] and M. D. Martínez-Rodrigo[1]

*Correspondence:
molinere@uji.es

[1] Department of Mechanical Engineering and Construction, Universitat Jaume I, Avda. Sos Baynat s/n, ES-12071 Castellón, Spain
[2] Escuela Técnica Superior de Ingeniería, Universidad de Sevilla, Camino de los descubrimientos s/n, ES-41092 Sevilla, Spain
[3] Laboratory of Engineering for Energy and Environmental sustainability, Universidad de Sevilla, Camino de los descubrimientos s/n, ES-41092 Sevilla, Spain

Abstract

This study investigates maximum vertical acceleration patterns in highly skewed, multi-span railway bridges, focusing on Serviceability Limit State (SLS) performance under increasing operational speeds. A 3D finite element model of a representative Spanish high-speed girder bridge is employed, explicitly incorporating the ballasted track and weak coupling between spans. The dynamic response is assessed using three train excitation models of increasing complexity: the simple moving load model (TLM), a vehicle-bridge interaction (VBI) model, and the latter incorporating track irregularities (VBI-η). The influence of deck skewness, modal participation, and ballast degradation at the simply-supported span interfaces is examined, along with a comparison to simplified analyses following code provisions. Quantitative results demonstrate that increasing deck skewness, from 90° to 134°, significantly reduces vertical accelerations by raising the first longitudinal bending and the first torsion frequencies, thus shifting prominent resonances outside the speed range of interest. While vehicle-bridge interaction (VBI) generally reduces accelerations at high speeds, track irregularities (VBI-η) can notably influence the maximum response depending on the speed window. The weak coupling between simply-supported spans affects spatial acceleration distribution, with maximum responses increasing near the supports. Additionally, localized ballast degradation at span interfaces impacts local peak accelerations. Comparisons show that code-based simplified models consistently overestimate accelerations above 300 km/h. These findings provide critical data for SLS compliance and speed upgrade assessments in multi-span skewed bridges.

Keywords: Railway bridges, Ballast track, Resonance, Weakly connected spans, Deck skewness, Vehicle-bridge interaction

1 Introduction

Growing concern about climate change has prompted the promotion of low-emission transport systems in modern societies. In this context, rail transport plays a pivotal role, providing a sustainable and efficient alternative for future mobility. The European Union (EU) is investing in the development of high-capacity, eco-efficient rail systems, as exemplified by initiatives such as Europe's Rail Joint Undertaking (Eu-Rail 2022). Simultaneously, the EU is committed to enhancing cross-border interoperability and harmonizing technical standards among member states—measures that are essential to improving the integration, efficiency, and competitiveness of the European rail network. Within this framework, high-speed (HS) railway bridges represent critical assets of rail infrastructure. It is well established that increases in circulating speed, vehicle axle loads, or variations in rolling stock axle spacing can induce significant vibrations in the deck platform, potentially compromising both structural stability and passenger comfort (ERRI 1999). Consequently, for speeds exceeding 200 km/h, the design of railway bridges—or their upgrading to accommodate new traffic conditions—requires dynamic analyses to verify serviceability in accordance with current regulations. In particular, EN 1990:2023 A2 (CEN 2023) prescribes a vertical deck acceleration limit of 3.5 m/s² for ballasted track bridges and 5 m/s² for non-ballasted bridges in the design of new structures. This requirement is especially restrictive for bridges with short to moderate spans, where the main structural elements typically consist of simply supported beams or plates (Frỳba 2004), making vertical acceleration one of the most stringent Serviceability Limit State (SLS) for traffic safety (Goicolea-Ruigómez 2007; Nasarre 2004).

The anticipated growth in railway transportation capacity, driven by sustainable mobility initiatives and interoperability efforts, has heightened the need for an accurate assessment of the dynamic compatibility between new or existing bridges and the rolling stock. The dynamic problem under consideration is inherently complex, as bridge deck vibrations are influenced by multiple factors, including the coupled behavior of the superstructure (Bornet et al. 2015; Saramago et al. 2022; Stollwitzer et al. 2023; Sánchez-Quesada et al. 2024)—comprising rails, ballast, and sleepers—the interaction with circulating vehicles (Arvidsson and Karoumi 2014), track irregularities (Peixer et al. 2021), and the surrounding soil (Zangeneh et al. 2018), among others. These effects are particularly pronounced in short- and skewed-span structures (Rocha et al. 2012). Accounting for these aspects typically requires complex, computationally intensive numerical analyses that depend heavily on the technical expertise of engineers. While existing design codes and regulations, such as the Eurocodes EN 1990:2023 A2, EN 1991-2:2024 (CEN 2023, 2023), provide recommendations and guidelines, their applicability is often debated under evolving traffic conditions (Arvidsson and Karoumi 2014; Ferreira et al. 2024; Museros et al. 2024). Although the modeling of railway bridge dynamic responses has advanced significantly over the past decades through increasingly sophisticated numerical approaches, evaluating the SLS for a large inventory of bridges—particularly for the approval of new train routes—remains a challenging task. Efficient and computationally streamlined models are therefore essential, with runtime cost being a critical consideration. Simple beam models have been widely used for dynamic analyses of railway bridges (Frỳba 1999; Yang et al. 1997; Johansson et al. 2014), under the assumption that the vibratory response is dominated by longitudinal bending modes. The European Standard EN 1991-2:2024 (CEN 2023) supports this simplification for simple structures when the frequency of the first torsional mode exceeds 1.2 times that of the first longitudinal bending mode.

However, oblique or skewed bridges are common in railway networks (Nguyen et al. 2019). These structures exhibit coupled bending–torsional behavior, which can be particularly pronounced in multi-track bridges due to track eccentricity (Martínez-Rodrigo et al. 2010; Galvín et al. 2018), and in bridges of short-to-moderate spans, where the span-to-width ratio approaches unity. Furthermore, bridges with open cross-sections (e.g., I-girder, T-beam, half-through, or U-type decks) typically have lower torsional stiffness compared to closed sections (e.g., box, U-girder decks, or voided slabs), often resulting in closely spaced bending and torsion natural frequencies—contrasting with the behavior of long beam-type viaducts (Galvín et al. 2021).

Scientific research still faces limitations in the comprehensive investigation of the dynamic performance of multi-span SS skewed bridges. Previous studies have primarily focused on modal characterization and dynamic analyses under simplified train load models. Moreover, most related works have examined bridge decks with closed cross-sections, which exhibit high torsional stiffness and minimal warping deformations (Nguyen et al. 2019; Agarwal et al. 2022). Only a few studies have integrated experimentally updated, detailed 3D FE models with a VBI framework that simultaneously accounts for track irregularities and a realistic representation of the ballasted track, simulating the weak coupling between the adjacent spans. These limitations continue to hinder progress in developing efficient predictive methodologies and refining guidelines aimed at ensuring the safe and cost-effective design of new bridges, the accurate assessment and maintenance of existing structures, and the rational use of engineering resources.

The present study aims to conduct a comprehensive investigation of the maximum vertical acceleration patterns in highly skewed, multi-span railway bridges, which exhibit a pronounced coupled flexural–torsional response, and to assess their compliance with SLS requirements under increasing operational speeds. The research focuses on an existing girder bridge from the Spanish HS network, used as a representative case study. However, the main conclusions derived from this work may also be applicable to other deck configurations with behavior comparable to that of an isotropic or orthotropic plate, in which the dynamic response is mainly governed by global deformation modes (i.e. longitudinal and transverse bending, torsion). Other typologies require a specific study that falls outside the scope of this work and may be of interest for future research.

The primary objective of the research is to analyze the maximum acceleration response and its spatial distribution across the ballast platform by systematically expanding the speed window of interest. This approach provides a general and innovative perspective, offering key insights for speed upgrading scenarios. It also enables the identification of predominant modal contributions to the maximum response within each speed range and supports conclusions regarding the level of refinement required in numerical models to achieve accurate SLS assessments.

The analysis is carried out using an unusually detailed 3D FE model that explicitly represents the ballasted track through an anisotropic formulation, including the weak coupling zones between structurally independent spans. The study compares the maximum acceleration under both normative trains and real rolling stock models, employing three approaches of increasing complexity: the simple TLM, the VBI model, and the VBI model incorporating track irregularities. The influence of bridge skewness and flexural-torsional coupled behavior on the dynamic response is examined. Furthermore, the sensitivity to ballast degradation at the span interfaces—representing weakened coupling—is evaluated to assess its impact on the overall structural response. Finally, a critical comparison is performed with a simplified orthotropic plate analysis, following

Eurocode-based recommendations for the assessment of SLS in skewed bridges, in order to quantify the level of over-prediction inherent to the normative approach.

The remainder of the article is organized as follows. Section 2 presents the reference bridge description and its experimentally identified modal parameters. Section 3 details the formulation of the train–track–bridge FE model, while Sect. 4 describes the dynamic analysis methodology. The results, along with a comprehensive discussion, are presented in Sect. 5. Finally, the main conclusions of the study are summarized in Sect. 6.

2 Railway bridge under study

In this section, the main geometric and dynamic characteristics of an existing railway bridge on the Madrid–Sevilla high-speed line in Spain are presented as a representative case study. The selected structure, built in the 1980 s (hereafter referred to as the Jabalón Bridge), consists of three identical SS spans of 24.9 m, crossing the Jabalón River at a skew angle of 134° (Fig. 1a). Each span comprises a double-track reinforced concrete slab 11.6 m wide, supported on five pre-stressed concrete I-girders, each 2.05 m in height. The girders rest on the supports—two outer reinforced concrete abutments and two inner wall piers—via laminated rubber bearings. The transverse displacement of the outer girders is additionally restrained by lateral bearings. At the supports, the ends of the I-girders are further braced by a transverse reinforced concrete beam of rectangular cross-section (Fig. 1b). A detailed description of the bridge dimensions and additional graphical information is provided in Sánchez-Quesada et al. (2024).

In May 2019, the authors conducted an experimental program to identify the modal parameters of the structure as well as the dynamic properties of the surrounding soil. Vertical accelerations beneath the longitudinal girders were measured under both ambient vibrations and operational conditions during several train passages. Due to accessibility constraints, instrumentation was limited to one of the end spans. A detailed description of the experimental procedure is provided in Galvín et al. (2021). From combined ambient and free vibrations after train passages, following the procedure described in Galvín et al. (2025), several natural frequencies below 30 Hz and their corresponding mode shapes were identified. These results are presented in Fig. 2.

From the identified mode shapes at the end span—including the first longitudinal bending, first torsion, first transverse bending, and additional coupled flexural–torsional modes—it is evident that the structure exhibits a pronounced three-dimensional

(a) General view. (b) Cross section.

Fig. 1 Jabalón Bridge

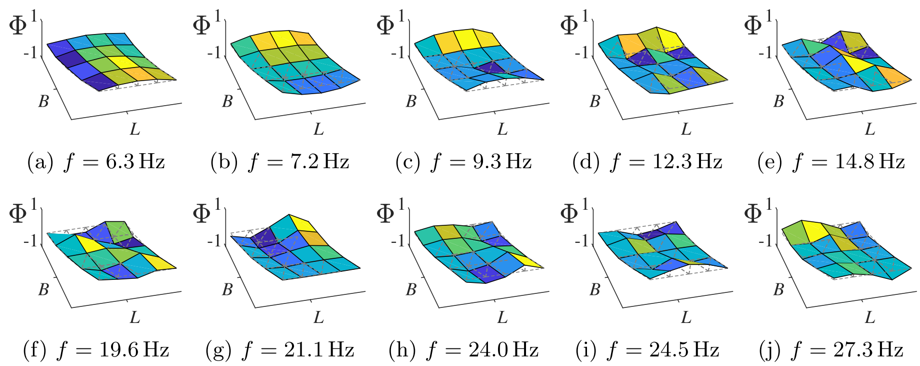

Fig. 2 Natural frequencies and mode shapes experimentally identified in Jabalón Bridge

behavior, distinct from the beam-type response typically observed in long viaducts. Dynamic tests on the surrounding soil allowed for the identification of the P-wave and S-wave velocities, revealing that the soil exhibits very high stiffness (Galvín et al. 2021).

3 Train-track-bridge numerical model

This section describes the numerical model developed to predict the vertical acceleration levels of the Jabalón Bridge under operational conditions. The model features a detailed discretization of the ballasted track, which connects all three simply-supported spans. Railway-induced excitation is modeled using a vehicle–bridge interaction approach based on multi-body dynamics, in addition to the simple TLM. In this framework, the bridge and vehicle subsystems are coupled through displacement relationships between the rails and wheels, assuming idealized, rigid contact.

3.1 Track-bridge FE model

A detailed linear elastic FE model of the bridge—including the three simply supported decks, the track superstructure (rails, ballast, sleepers, and rail pads), the elastomeric bearings at the supports, and the mass of additional non-structural elements (e.g., handrails)—is implemented in ANSYS 2023 R1 (Fig. 3). The piers and abutments are not included, nor is the soil, which exhibits very high stiffness according to experimental measurements.

The structural components of the decks (slab, longitudinal, and transverse girders) are modeled using isotropic Reissner–Mindlin shell elements with four nodes (SHELL181) and six degrees of freedom (DOFs) per node, allowing accurate representation of the three-dimensional slab deformation while maintaining computational efficiency. Laminated rubber bearings beneath the longitudinal girders are discretized with eight-node hexahedral solid elements (SOLID185), with dimensions obtained from technical drawings (INTEMAC 1991), and are assigned three DOFs per node. The vertical displacements of nodes on the lower surface of the bearings are constrained, fixed-support conditions. Horizontal bearings are represented using discrete one-dimensional spring elements (COMBIN14).

The ballast track constitutes a fundamental element in the transmission of forces from vehicle wheels to the bridge deck. Additionally, in bridges composed of multiple simply supported spans, a weak coupling develops between the spans due to

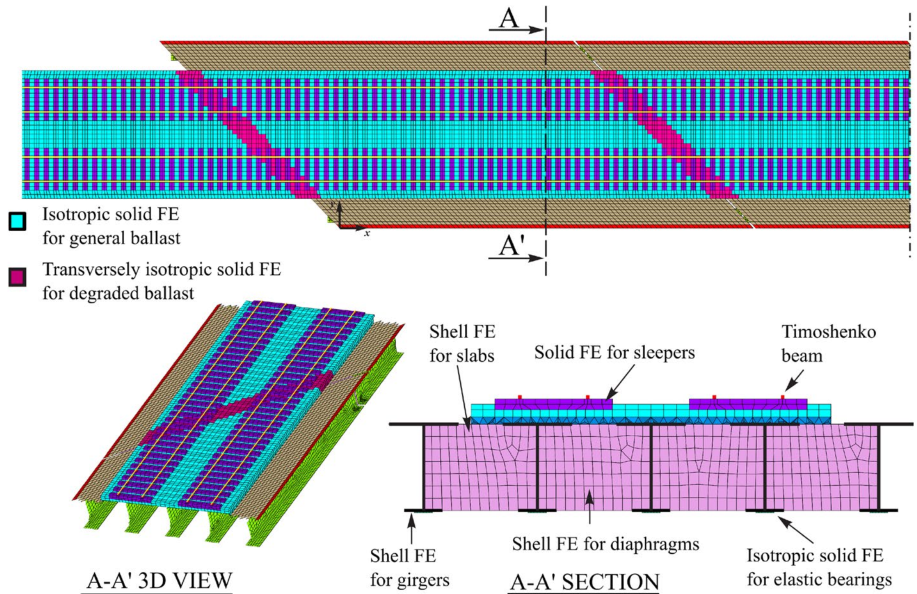

Fig. 3 FE model of Jabalón Bridge

the continuity of the track. In the scientific literature, specific computational techniques, such as the discrete element method (DEM), are applied in geotechnics to study particular ballast-related problems arising from its granular nature, e.g., ballast settlement, breakage, degradation under cyclic loads, ballast–sleeper interaction, and lateral track resistance (Aela et al. 2025; Khatibi et al. 2017; Chen et al. 2023; Guo et al. 2020). However, applying DEM to large-scale structures or macro-scale problems, such as the assessment of the SLS in railway bridges, is computationally prohibitive due to the excessive time required (Jia et al. 2023).

Consistent with previous research on railway bridge dynamics (Nguyen et al. 2012; Xiao et al. 2020; Saramago et al. 2022), a continuum-based approach for the ballast layer is adopted. The ballast volume is meshed with solid FE elements (SOLID185), as shown in Fig. 3. Two constitutive models are used: near the transverse joints between spans, a transversely isotropic material is assigned, while the remaining ballast volume is considered isotropic. This approach captures the distinct interlocking mechanisms of ballast granules in the vertical and horizontal directions at the interfaces between the successive SS spans. Previous studies highlight the potential degradation of ballast mechanical properties in these transition regions due to cyclic movements induced by train passages (Ticona Melo et al. 2020; Bonifácio et al. 2014).

Additional key track elements, such as concrete sleepers, are also meshed with SOLID185 elements assuming isotropic behavior. Rails are modeled as Timoshenko beam elements with two nodes and six DOFs per node (BEAM188), improving accuracy at higher frequencies compared to Bernoulli–Euler elements. Rail pads are simulated as one-directional discrete spring elements (COMBIN14) with constant vertical stiffness, connecting the relative vertical displacements between rails and sleepers. Non-structural elements, including handrails and sidewalks, are represented as additional masses distributed over their contributive regions.

To minimize boundary effects, the track extends 15 m onto the embankment on both sides of the bridge. Convergence analysis on the numerical mode shapes verifies the adequacy of this extension. In these regions, the track rests on a subgrade layer meshed with SOLID185 elements assuming isotropic behavior, and the nodes at the horizontal lower plane of this layer are restrained.

The FE model undergoes an automated updating procedure to reproduce the experimentally identified natural frequencies and mode shapes. Model calibration involves two main steps. First, a preliminary sensitivity analysis identifies the parameters most influential on the natural frequencies and mode shapes, with initial values taken from technical drawings (INTEMAC 1991) and the literature. Second, the subset of relevant parameters is calibrated using a genetic algorithm. Further details on the track–bridge FE model and the updating procedure are provided in Sánchez-Quesada et al. (2024).

Table 1 summarizes the final (calibrated) parameter values. E and ν denote the elastic modulus and Poisson's ratio of the various bridge components, respectively. For mass properties, ρ represents mass density, m the linearly distributed mass, and M the total mass. I_{yr} indicates the second moment of area of the UIC60 rail cross-section about the Y axis (see Fig. 3). For components modeled as linear springs (rail pads and horizontal bearings), K represents the adopted discrete stiffness. Sleeper dimensions—length (l_{sl}), width (w_{sl}), and height (h_{sl})—are provided, with d_{sl} denoting the distance between consecutive sleepers. Vertical bearing dimensions follow the same notation.

The total ballast thickness is $h_b + h_{sl}/2$, admitted constant and uniform over the platform, with h_b beneath the sleepers. In the degraded ballast regions, the five independent elastic constants defining transversely isotropic behavior are included: $E_{bX} = E_{bY}$ (in-plane elastic moduli), E_{bZ} (out-of-plane elastic modulus), $G_{bXZ} = G_{bYZ}$ (out-of-plane shear moduli), and Poisson's ratios ν_{bXY} and $\nu_{bXZ} = \nu_{bYZ}$. The calibrated values in Table 1 show a reduction of in-plane elastic constants relative to E_{bZ}. Finally, for the elastic bearings, R_{eb} and R_{ebt} are factors applied to the vertical and transverse bearing moduli under dynamic loading.

3.2 Train excitation

In this study, railway excitation is introduced under two approaches: (i) the simple TLM approach, in which the vehicle axle loads are represented as point forces moving at constant speed; and (ii) the VBI model, which represents the train as a three-dimensional multi-body system of rigid masses connected by linear springs and dampers. This latter approach allows capturing not only the inertial effects of the vehicle masses and the energy dissipation provided by the suspension systems, but also the dynamic interaction forces between the track and the vehicle arising from track irregularities.

Two types of trains are considered: articulated and regular. First, the normative High-Speed Load Model A (HSLM-A) defined in the European Standard EN 1991-2:2024 for design purposes, which consists of ten articulated trains with varying axle loads and carriage lengths, intended to be an envelope of the effects of existing HS trains. In addition, two real trains that regularly operate on Jabalón Bridge line are analyzed: the articulated RENFE S100 and the regular RENFE S102 trains. The first real train is directly derived from the TGV Atlantique and consists of two power cars, each with two motorized bogies, along with eight passenger cars with shared bogies. The second train comprises

Table 1 Updated model parameters of Jabalón Bridge (Sánchez-Quesada et al. 2024)

Bridge component	Notation	Value	Unit
Rail UIC60	E_r	$2.10 \cdot 10^{11}$	Pa
	I_{yr}	$3038 \cdot 10^{-8}$	m^4
	m_r	60.34	kg/m
Rail pads	K_p	$1.00 \cdot 10^8$	N/m
Sleepers	E_{sl}	$3.60 \cdot 10^{10}$	Pa
	ν_{sl}	0.3	-
	w_{sl}	0.30	m
	l_{sl}	2.60	m
	h_{sl}	0.24	m
	M_{sl}	320	kg
	d_{sl}	0.60	m
Ballast	h_b	0.35	m
	E_b	$5.70 \cdot 10^7$	Pa
	ν_b	0.3	-
	ρ_b	1700	kg/m^3
Degraded ballast	$E_{bX} = E_{bY}$	$3.42 \cdot 10^7$	Pa
	E_{bZ}	$5.46 \cdot 10^7$	Pa
	$G_{bYZ} = G_{bXZ}$	$1.33 \cdot 10^7$	Pa
	$\nu_{bXY}=\nu_{bYX}$	0.3	-
	$\nu_{bXZ}=\nu_{bYZ}$	0.3	-
	ρ_b	1700	kg/m^3
Subgrade	E_f	$9.00 \cdot 10^7$	Pa
	ν_f	0.3	-
	ρ_f	1800	kg/m^3
Girders	E_g	$3.80 \cdot 10^{10}$	Pa
	ν_g	0.2	-
	ρ_g	2645	kg/m^3
Slabs	E_s	$2.60 \cdot 10^{10}$	Pa
	ν_s	0.2	-
	ρ_s	2698	kg/m^3
Diaphragms	E_{dph}	$2.60 \cdot 10^{10}$	Pa
	ν_{dph}	0.2	-
	ρ_{dph}	2698	kg/m^3
Handrails	m_h	50	kg/m
Sidewalks	m_{sw}	195	kg/m
Vertical bearings	E_{eb}	$4.83 \cdot 10^7$	Pa
	ν_{eb}	0.49	-
	ρ_{eb}	1230	kg/m^3
	R_{eb}	2.00	-
	w_{eb}	0.40	m
	l_{eb}	0.33	m
	h_{eb}	0.049	m
Horizontal bearings	K_{eb}	$5.56 \cdot 10^7$	N/m
	R_{ebt}	2.00	-

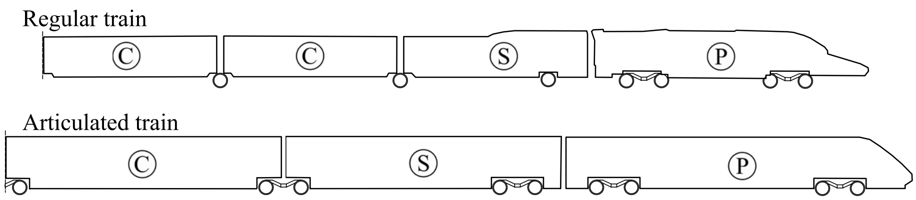

Fig. 4 Regular (RENFE S102) and articulated (HSLM-A & RENFE S100) trains. Initials P, S, C denote power, side, and central car, respectively

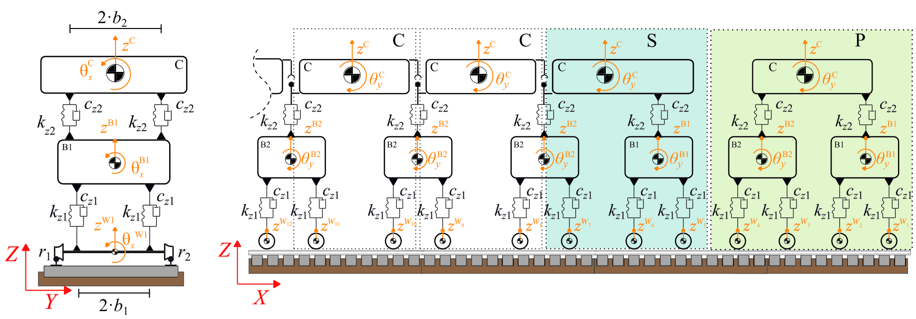

(a) Front view. (b) Lateral view.

Fig. 5 VBI model sketch for articulated trains

12 typical single-axle TALGO passenger coaches, modified to allow speeds of up to 330 km/h, with power cars at each end. Both trains are currently used in Spanish high-speed services. Figure 4 provides a schematic representation of both, which exhibit symmetrical axle load distributions.

The TLM axle loads and spacings can be found in EN 1991-2:2024 (CEN 2023) for the HSLM-A trains and in Sánchez-Quesada (2025) for the real trains. For clarity, these values are also provided in Appendix 1. Figure 5 presents front and side view schematics of the VBI model used in this work for the articulated trains (HSLM-A and RENFE S100), which represents car bodies, bogies, and wheelsets as rigid masses interconnected by spring-dashpot elements.

Each car body and bogie has three DOFs: vertical displacement (z^{C} and $z^{\mathrm{B}i}$, respectively), rolling (θ_x^{C} and $\theta_x^{\mathrm{B}i}$), and pitching (θ_y^{C} and $\theta_y^{\mathrm{B}i}$). Each wheelset has two DOFs: vertical displacement (z^{W_i}) and rolling ($\theta_x^{W_i}$). Power cars consist of a single car body and two independent bogies, totaling 17 DOFs each. Side cars feature one independent (non-articulated) bogie and share an articulated bogie with the adjacent carriage, while the remaining passenger cars share both bogies with neighboring carriages. The hinge between car bodies is modeled as a vertically stiff connection, coupling the vertical displacement of each car body with the vertical and pitching motions of the preceding one.

The VBI model of the regular train RENFE S102 follows the same structure, with the difference that in the passenger carriages, each bogie has only two DOFs (vertical displacement $z^{\mathrm{B}i}$ and rolling $\theta_x^{\mathrm{B}i}$) and a single wheelset. A detailed description of the mass, damping, and stiffness matrices for both the articulated and regular train VBI models is provided in Sánchez-Quesada (2025). Appendix 2 provides the train matrices used in this work in closed form. Previous research provides further alternatives for deriving these matrices, such as utilizing commercial FE packages (Ferreira et al. 2024).

The mechanical parameters required to implement the VBI version of the HSLM-A trains are analogous to those included in Arvidsson et al. (2018); Ferreira et al. (2024). In Arvidsson et al. (2018), the authors develop a 2D multi-body model by adjusting the car body masses to match the axle loads of the ten trains (ranging from 17 to 21 t/axle) and by tuning the primary and secondary suspension characteristics to reproduce realistic bounce frequencies. In Ferreira et al. (2024), additional parameters are introduced to extend the model to three dimensions. For the sake of completeness, the adopted values for the HSLM-A trains from these sources, as well as the mechanical properties used for the real trains RENFE S102 and RENFE S100, are provided in Appendix 1.

3.3 Track irregularities

In the VBI $-\ \eta$ model track irregularities with wavelengths in the range $[3-25]\,m$ are considered to model the coupling between the wheelsets and the rails. This wavelength range corresponds to the D1 class defined in EN 13848-5:2017 (CEN 2018), since it is considered more relevant for running safety and structural assessment (Cantero et al. 2016). The irregularities are generated from the analytical power spectral density (PSD) functions of the vertical profile, $S_V(\Omega)$, and the cross level, $S_C(\Omega)$, as provided in Claus and Schiehlen (1998). They are defined according to

$$S_V(\Omega) = A\frac{\Omega_c^2}{(\Omega_r^2+\Omega^2)(\Omega_c^2+\Omega^2)} \quad S_C(\Omega) = \frac{A}{(l/2)^2}\frac{\Omega_c^2\Omega^2}{(\Omega_r^2+\Omega^2)(\Omega_c^2+\Omega^2)(\Omega_s^2+\Omega^2)}, \tag{1}$$

where Ω is the wavenumber (rad/m); Ω_r, Ω_c, and Ω_s are the truncated frequencies (rad/m); A is a roughness factor (rad m); and l_v is the distance between the rails (m). The same values adopted in Claus and Schiehlen (1998) are used in this study: $\Omega_r = 0.0206\,\text{rad/m}$, $\Omega_c = 0.8246\,\text{rad/m}$, $\Omega_s = 0.4380\,\text{rad/m}$, $A = 0.79305\cdot 10^{-6}\,\text{rad m}$, and $l_v = 1.435\,\text{m}$. Next, the spatial samples representing the track irregularity profile are generated using the spectral representation method, with the function

$$r_i(x) = \sum_{n=1}^{N}\sqrt{\frac{2}{\pi}S_i(\Omega_n)\Delta\Omega}\cdot\cos(\Omega_n\cdot x-\beta_n), \tag{2}$$

where $i = V, C$ denotes the vertical alignment and the cross-level, respectively. Ω_n are discrete spatial frequencies evenly spaced within the interval $\Omega_L = 2\pi/25\,\text{rad/m}$ and $\Omega_U = 2\pi/3\,\text{rad/m}$. The sampling frequency is defined as $\Delta\Omega = (\Omega_U-\Omega_L)/N$, with N representing the number of harmonics used to generate the irregularity profile. β_n is a random phase angle uniformly distributed within the interval $[0, 2\pi]\,\text{rad}$. Finally, the vertical irregularity profiles for the right and left rails ($\eta_{r_1}(x)$ and $\eta_{r_2}(x)$, respectively) are defined as

$$\eta_{r_1}(x) = r_V(x) + r_C(x)/2 \qquad \eta_{r_2}(x) = r_V(x) - r_C(x)/2. \tag{3}$$

Figure 6 presents the track irregularity profiles considered in this study. The zero-to-peak values of isolated defects along the longitudinal level remain below the intervention alert limits specified in EN 13848-5:2017 (CEN 2018). The standard deviation of the

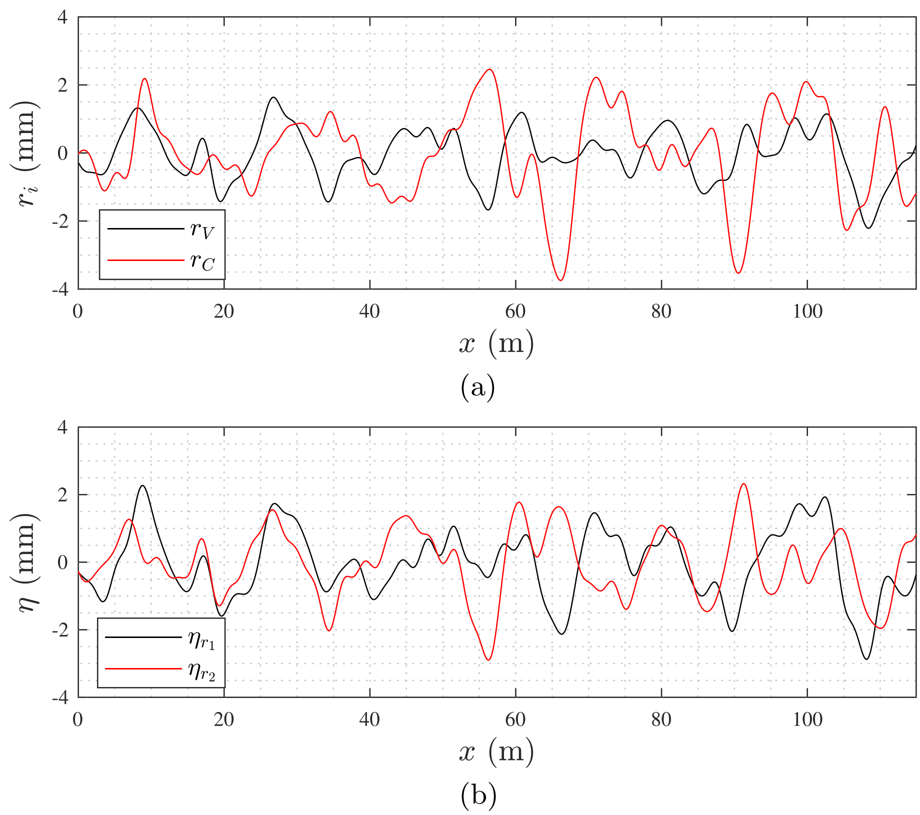

Fig. 6 Generated irregularity profiles: **a** Vertical profiles r_V and cross levels r_C; **b** Vertical track irregularities for right and left rails, η_{r_1} and η_{r_2}

longitudinal level, calculated as $(\sigma(\eta_{r_1}) + \sigma(\eta_{r_2}))/2$, is 1.0142 mm, which corresponds to a Type D track according to EN 13848-6:2014+A1:2020 (CEN 2020).

3.4 Coupled equations of motion

The dynamic response of the bridge under train loads is computed by transforming the track–bridge FE equilibrium equations into modal space:

$$\mathbf{M}_b \cdot \ddot{\boldsymbol{\xi}} + \mathbf{C}_b \cdot \dot{\boldsymbol{\xi}} + \mathbf{K}_b \cdot \boldsymbol{\xi} = -{\boldsymbol{\Psi}_r}^{\mathrm{T}} \cdot \mathbf{F}_{int} \tag{4}$$

where $\mathbf{M}_b$, $\mathbf{C}_b$ and $\mathbf{K}_b$ are the modal mass, damping and stiffness matrices, $\boldsymbol{\xi}$ is the vector of generalized coordinates; $\mathbf{F}_{int}$ denotes the wheel-rail interaction forces, and $\boldsymbol{\Psi}_r$ are the undamped mode shapes of the bridge model evaluated at the wheel–rail contact points (superscript T denotes transpose) using FE interpolation. In this work, the undamped mode shapes are retrieved from ANSYS normalized to mass matrix. Therefore, $\mathbf{M}_b$ corresponds to the identity matrix, $\mathbf{K}_b(j,j) = \omega_j^2$ is a diagonal matrix with ω_j being the j–th natural frequency, and a viscous modal damping approach is admitted so that $\mathbf{C}_b(j,j) = 2\zeta_j \cdot \omega_j$ is also diagonal.

In the TLM train model, $\mathbf{F}_{int}$ represents the concentrated axle loads. The bridge response under operating conditions is obtained by solving the system of equations (Eq. 4) using the implicit Newmark-Beta integration scheme. Modal contributions up to 30 Hz are included, according to EN 1990:2023 A2.

The VBI model for the train excitation requires the solution of two coupled systems of equations: those governing the response of the track-bridge system (Eq. 4) and the train dynamics, expressed as

$$\begin{bmatrix} \mathbf{M}_v & 0 \\ 0 & \mathbf{M}_w \end{bmatrix} \cdot \begin{bmatrix} \ddot{\mathbf{x}}_v \\ \ddot{\mathbf{x}}_w \end{bmatrix} + \begin{bmatrix} \mathbf{C}_v & \mathbf{C}_{vw} \\ \mathbf{C}_{vw}^{\mathrm{T}} & \mathbf{C}_w \end{bmatrix} \cdot \begin{bmatrix} \dot{\mathbf{x}}_v \\ \dot{\mathbf{x}}_w \end{bmatrix} + \begin{bmatrix} \mathbf{K}_v & \mathbf{K}_{vw} \\ \mathbf{K}_{vw}^{\mathrm{T}} & \mathbf{K}_w \end{bmatrix} \cdot \begin{bmatrix} \mathbf{x}_v \\ \mathbf{x}_w \end{bmatrix} = \begin{bmatrix} \mathbf{P}_v \\ \mathbf{P}_w + \mathbf{F}_{int} \end{bmatrix} \tag{5}$$

where $\mathbf{x}_v$, $\mathbf{x}_w$ are the DOFs of the car bodies/bogies and wheelsets, $\mathbf{P}_v$ and $\mathbf{P}_w$ their self-weights, and $\mathbf{M}_i$, $\mathbf{C}_i$, $\mathbf{K}_i$ $(i = v, w)$ are the corresponding direct mass, damping and stiffness matrices, with $\mathbf{C}_{vw}$ and $\mathbf{K}_{vw}$ representing cross-coupling. The complete description of Eq. 5 can be consulted in Sánchez-Quesada (2025) and in Appendix 2. Finally, Eqs. 4 and 5 are coupled via wheel–rail compatibility, assuming direct contact and considering only convective terms from track irregularities (Zhang et al. 2010; Guo et al. 2012). In virtue of the previous assumptions, the DOFs of each wheelset $(z^{W_i}, \theta_x^{W_i})$ are related with the vertical displacements of the right and left rails $z_{r_1}^{W_i}$ and $z_{r_2}^{W_i}$ as follows,

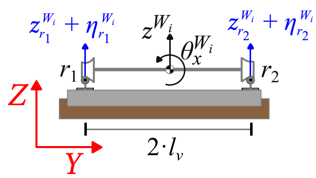

$$\begin{bmatrix} z^{W_i} \\ \theta_x^{W_i} \end{bmatrix} = \begin{bmatrix} 1/2 & 1/2 \\ -1/l_v & 1/l_v \end{bmatrix} \cdot \begin{bmatrix} z_{r_1}^{W_i} + \eta_{r_1}^{W_i} \\ z_{r_2}^{W_i} + \eta_{r_2}^{W_i} \end{bmatrix} \qquad \mathbf{x}^{W_i} = \mathbf{T}^{W_i} \cdot (\boldsymbol{z}^{W_i} + \boldsymbol{\eta}^{W_i}) \tag{6}$$

where $\eta_{r_k}^{W_i}$ stands for the vertical irregularity profile at the contact point of each rail, as per Eq. 3. The vertical displacements of the rails at the contact points $z_{r_k}^{W_i}$ are obtained by the superposition of N_{mod} mode shapes

$$z_{r_k}^{W_i} = \sum_{j=1}^{N_{mod}} \left(\psi_{r_k,j}^{W_i} \cdot \xi_j \right) \qquad \psi_{r_k,j}^{W_i} = \mathbf{N}_{r_k}^{e,W_i} \cdot \breve{\boldsymbol{\psi}}_{r_k,j}^{e,W_i} \tag{7}$$

where $\psi_{r_k,j}^{W_i}$ is the vertical amplitude associated to the j–th mode of vibration at the contact point in each rail, which is obtained by FE using the element shape function $\mathbf{N}_{r_k}^{e,W_i}$ between its nodal mode shapes $\breve{\boldsymbol{\psi}}_{r_k,j}^{e,W_i}$ obtained from FE model.

Finally, extending Eqs. 6 and 7 to the N_w wheelsets of the passing trains, a coupled system of equations that permits the calculation of the displacements of the bridge and the car bodies/bogies is obtained:

$$\begin{bmatrix} \mathbf{M}_v & 0 \\ 0 & \mathbf{M}_b + \boldsymbol{\Phi}^{\mathrm{T}} \cdot \mathbf{M}_w \cdot \boldsymbol{\Phi} \end{bmatrix} \cdot \begin{bmatrix} \ddot{\mathbf{x}}_v \\ \ddot{\boldsymbol{\xi}} \end{bmatrix} + \begin{bmatrix} \mathbf{C}_v & \mathbf{C}_{vw} \cdot \boldsymbol{\Phi} \\ \boldsymbol{\Phi}^{\mathrm{T}} \cdot \mathbf{C}_{vw}^{\mathrm{T}} & \mathbf{C}_b + \boldsymbol{\Phi}^{\mathrm{T}} \cdot \mathbf{C}_w \cdot \boldsymbol{\Phi} \end{bmatrix} \cdot \begin{bmatrix} \dot{\mathbf{x}}_v \\ \dot{\boldsymbol{\xi}} \end{bmatrix} + \begin{bmatrix} \mathbf{K}_v & \mathbf{K}_{vw} \cdot \boldsymbol{\Phi} \\ \boldsymbol{\Phi}^{\mathrm{T}} \cdot \mathbf{K}_{vw}^{\mathrm{T}} & \mathbf{K}_b + \boldsymbol{\Phi}^{\mathrm{T}} \cdot \mathbf{K}_w \cdot \boldsymbol{\Phi} \end{bmatrix} \cdot \begin{bmatrix} \mathbf{x}_v \\ \boldsymbol{\xi} \end{bmatrix} = \begin{bmatrix} \mathbf{P}_t \\ \boldsymbol{\Phi}^{\mathrm{T}} \cdot \mathbf{P}_b \end{bmatrix} \tag{8}$$

where $\boldsymbol{\Phi} = \mathbf{T} \cdot \boldsymbol{\Psi}_r$. The matrix $\mathbf{T}$ is the transformation matrix of Eq. 6 extended to the N_w wheelsets as follows,

$$\mathbf{T} = \mathit{diagonal}\,[\mathbf{T}^{W_1} \quad \mathbf{T}^{W_2} \quad \ldots \quad \mathbf{T}^{W_i} \quad \ldots \quad \mathbf{T}^{W_{Nw}}] \tag{9}$$

Matrix $\mathbf{\Psi}_r$, previously introduced in Eq. 4, depends on the position of the train and therefore needs to be updated each time step. It is defined as,

$$\mathbf{\Psi}_r = \begin{bmatrix} \psi_{r_1,1}^{W_1} & \cdots & \psi_{r_1,j}^{W_1} & \cdots & \psi_{r_1,N_{mod}}^{W_1} \\ \psi_{r_2,1}^{W_1} & \cdots & \psi_{r_2,j}^{W_1} & \cdots & \psi_{r_2,N_{mod}}^{W_1} \\ \vdots & \ddots & & & \vdots \\ \psi_{r_1,1}^{W_i} & \cdots & \psi_{r_1,j}^{W_i} & \cdots & \psi_{r_1,N_{mod}}^{W_i} \\ \psi_{r_2,1}^{W_i} & \cdots & \psi_{r_2,j}^{W_i} & \cdots & \psi_{r_2,N_{mod}}^{W_i} \\ \vdots & & & \ddots & \vdots \\ \psi_{r_1,1}^{W_{Nw}} & \cdots & \psi_{r_1,j}^{W_{Nw}} & \cdots & \psi_{r_1,N_{mod}}^{W_{Nw}} \\ \psi_{r_2,1}^{W_{Nw}} & \cdots & \psi_{r_2,j}^{W_{Nw}} & \cdots & \psi_{r_2,N_{mod}}^{W_{Nw}} \end{bmatrix} \tag{10}$$

Finally, vector $\mathbf{P}_b$ collects the dynamic interaction forces between the rails and the vehicles, which are zero if track irregularities are neglected, as well as the gravitational vertical loads of the wheelsets. In a similar way, vector $\mathbf{P}_t$ contains the gravity loads of the car bodies and bogies, as well as the dynamic interaction forces due to track irregularities. They are defined as follows,

$$\mathbf{P}_t = \mathbf{P}_v - \mathbf{C}_{vw} \cdot \mathbf{T} \cdot \dot{\boldsymbol{\eta}} - \mathbf{K}_{vw} \cdot \mathbf{T} \cdot \boldsymbol{\eta} \tag{11}$$

$$\mathbf{P}_b = \mathbf{P}_w - \mathbf{M}_w \cdot \mathbf{T} \cdot \ddot{\boldsymbol{\eta}} - \mathbf{C}_w \cdot \mathbf{T} \cdot \dot{\boldsymbol{\eta}} - \mathbf{K}_w \cdot \mathbf{T} \cdot \boldsymbol{\eta} \tag{12}$$

In the previous equations, $\boldsymbol{\eta}$ is a column vector that contains the vertical irregularity profile of the railway track at the contact points extended to the N_w wheelsets,

$$\boldsymbol{\eta} = \text{column}\left[\boldsymbol{\eta}^{W_1} \quad \boldsymbol{\eta}^{W_2} \quad \ldots \quad \boldsymbol{\eta}^{W_i} \quad \ldots \quad \boldsymbol{\eta}^{W_{Nw}}\right] \tag{13}$$

The nonlinear system of equations (Eq. 8) is also solved by direct numerical integration in the time domain using the Newmark-Beta implicit algorithm.

4 Methodology

In the following section, the evolution of the bridge's vertical acceleration response over the platform area is analyzed as the speed window is extended. The Jabalón Bridge FE model—updated using experimental measurements, as referenced in Sect. 3.1—is taken as the reference case. Several model configurations are considered, including straight and skewed variants, as well as single-span and three-span versions. Train excitation is represented through three different approaches: TLM, VBI and VBI–η.

The equations of motion are integrated in the time domain, considering the contribution of modes below 30 Hz, according to the European Standard EN 1990:2023 A2. Modal damping ratios are assigned according to EN 1991-2:2024 (CEN 2023). For each train passage, the bridge response is computed at 25 post-processing points per span, uniformly distributed along the ballast platform. Uppercase letters A to E (see Fig. 7) denote points along the first span in the train direction, F to J those along the second span, and K to O those on the third and exit span of the viaduct. In the following analysis, axle loads are assumed to be evenly distributed along both rail lines, with trains

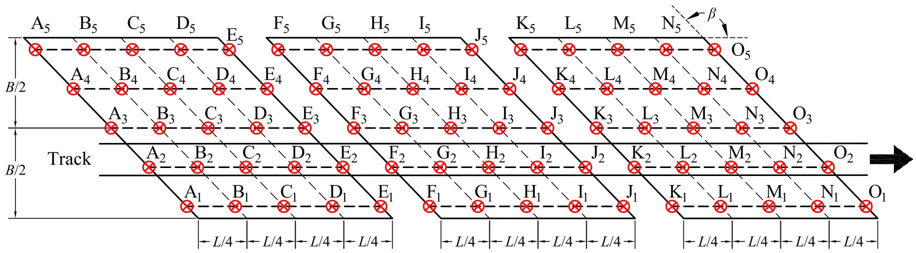

Fig. 7 Post-process points at each span

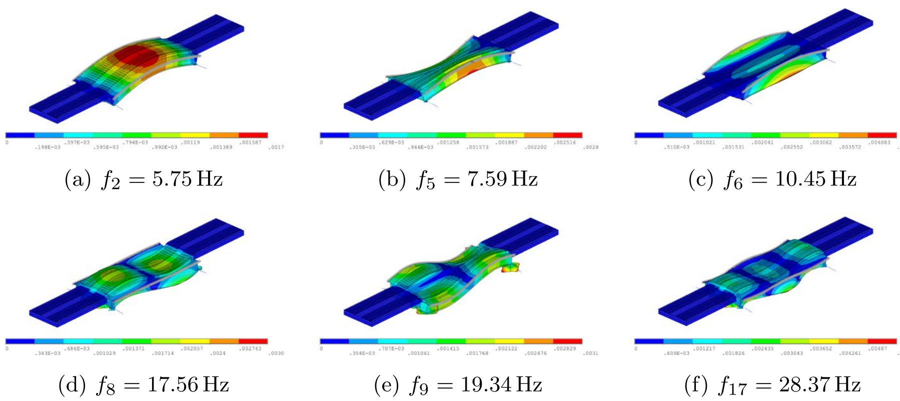

Fig. 8 Numerical mode shapes identified in single-span, straight (β=90°) model under 30 Hz

traveling at a constant speed. Regardless of the number of spans, the models always include the 15 m track extensions on either side of the bridge.

5 Results

5.1 Influence of the train model on the bridge vertical acceleration response

In this subsection, single-span, non-skewed versions of the Jabalón Bridge FE model are considered. Figure 8 illustrates six of the 19 normal mode shapes with frequencies below 30 Hz that are accounted for in the subsequent dynamic analyses. Longitudinal bending, torsional, and transverse bending modes alternate as the frequency increases.

In Fig. 9a-c, the overall maximum vertical acceleration of the deck for the ten HSLM-A trains at each post-processing point is shown as the upper speed limit, V_{lim}, increases. To generate this plot, the bridge's dynamic vertical response is computed for each train at multiple circulating speeds within the interval [144, V_{lim}] km/h, using a speed increment of $\Delta V = 3.6$ km/h. As the speed window is progressively extended, new resonances are accommodated, which may contribute to the overall maximum vertical response. Subfigures (a), (b), and (c) correspond to the three excitation modeling strategies: TLM, VBI, and VBI-η, respectively. Only acceleration values exceeding 3.5 m/s^2 are highlighted in colour.

Finally, Fig. 9d shows the maximum acceleration envelope for the 25 post-processing points as a function of the upper speed limit V_{lim}. At very low speeds, there is no noticeable difference in the response predictions among the three train models. When irregularities are neglected, vehicle-bridge interaction consistently results in lower bridge

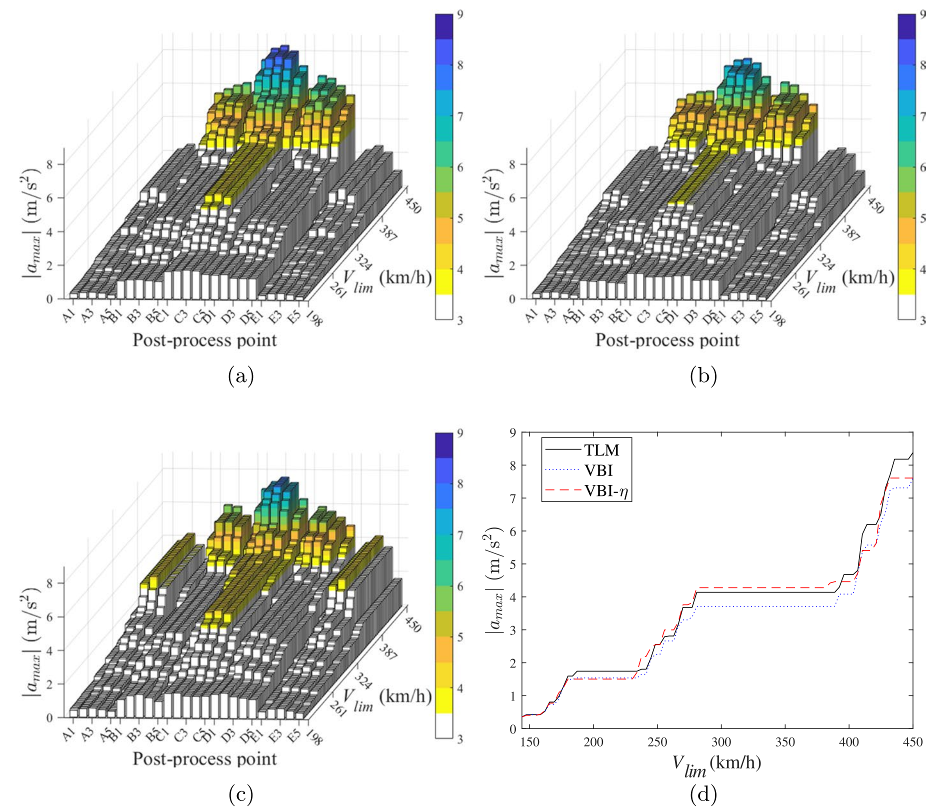

Fig. 9 Jabalón Bridge single-span model. Maximum acceleration under HSLM-A train passages vs. V_{lim}, under **a** TLM approach; **b** VBI and **c** VBI-η. **d** Maximum acceleration envelopes for the 25 post-process points

accelerations. When irregularities are considered, the excitation model producing the overall maximum response may depend on the speed window and the irregularity profile. It should be noted that track unevenness has a stochastic nature, and the results presented here correspond to a single realization. Therefore, a comprehensive statistical analysis would be required to rigorously quantify its effects. It should be also emphasized that only the overall maximum response is evaluated here. The influence of irregularities near the supports is more pronounced, although the absolute response at these locations remains relatively low.

5.2 Influence of the deck skewness on the bridge vertical response

Next, the effect of deck skewness on the maximum vertical acceleration is analyzed. In this section, the Jabalón Bridge model is still limited to a single span, with the angle β between the track longitudinal axis and the support line (see Fig. 7) defining the deck skewness; $\beta = 90°$ corresponds to a straight deck. Figure 10 compares the vertical acceleration envelope under HSLM-A TLM trains for the straight and skewed ($\beta = 134°$) configurations. In the skewed case, 23 modes with natural frequencies below 30 Hz are included in the response integration.

The vertical acceleration of the bridge decreases with increasing skewness at all post-processing points. This reduction is partly due to the increase in natural frequencies as the deck becomes skewed (Sánchez-Quesada et al. 2024). In this case, the first bending

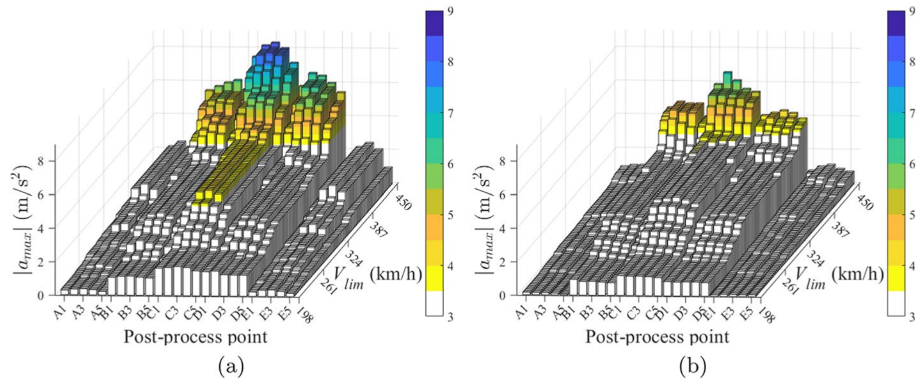

Fig. 10 Jabalón Bridge single-span models. Maximum acceleration under HSLM-A, TLM trains for (**a**) straight β=90° and (**b**) skewed β=134° cases

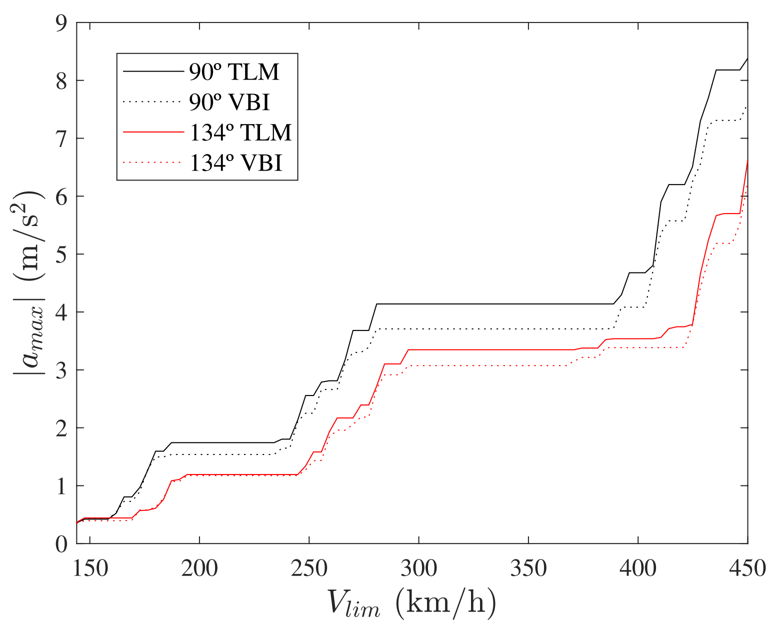

Fig. 11 Jabalón Bridge single-span models. Vertical acceleration envelopes vs. V_{lim} under HSLM–A trains

and first torsional frequencies rise from 5.76 Hz to 6.07 Hz and from 7.60 Hz to 7.93 Hz, respectively. Since the resonant speeds are proportional to the bridge frequencies f_i (i.e., $V^R_{i,j} = \frac{f_i \cdot d}{j}$, where d is the train characteristic distance and j the resonance order), the corresponding resonant speeds increase proportionally. This effect is illustrated in Fig. 11, where the acceleration envelope at the 25 post-processing points is plotted against the upper speed limit for both straight and skewed decks, and for both the HSLM-A TLM and HSLM-A VBI models.

The overall maximum acceleration, considering all post-processing points, exhibits a similar trend as the speed window is extended. However, two effects can be observed: on the one hand, the plateaus that appear when certain mode resonances are reached shift to higher speeds for the different trains, reflecting the increase in natural frequencies. On the other hand, the overall maximum response decreases, and the difference between the straight and skewed configurations becomes more pronounced as V_{lim} increases.

Finally, the influence of vehicle suspensions in the skewed case follows a similar pattern, consistently reducing the structural response, with a more significant effect at higher speeds. This behavior is expected because lower-order resonances occur at higher velocities, and resonance effects are most pronounced in these modes due to the lack of load-free cycles.

Next, the bridge in its skewed, single-span configuration is analyzed under the circulation of the two real trains: RENFE S100 and RENFE S102. Figure 12a, c, e, show the maximum bridge acceleration under the RENFE S100 as the speed window is

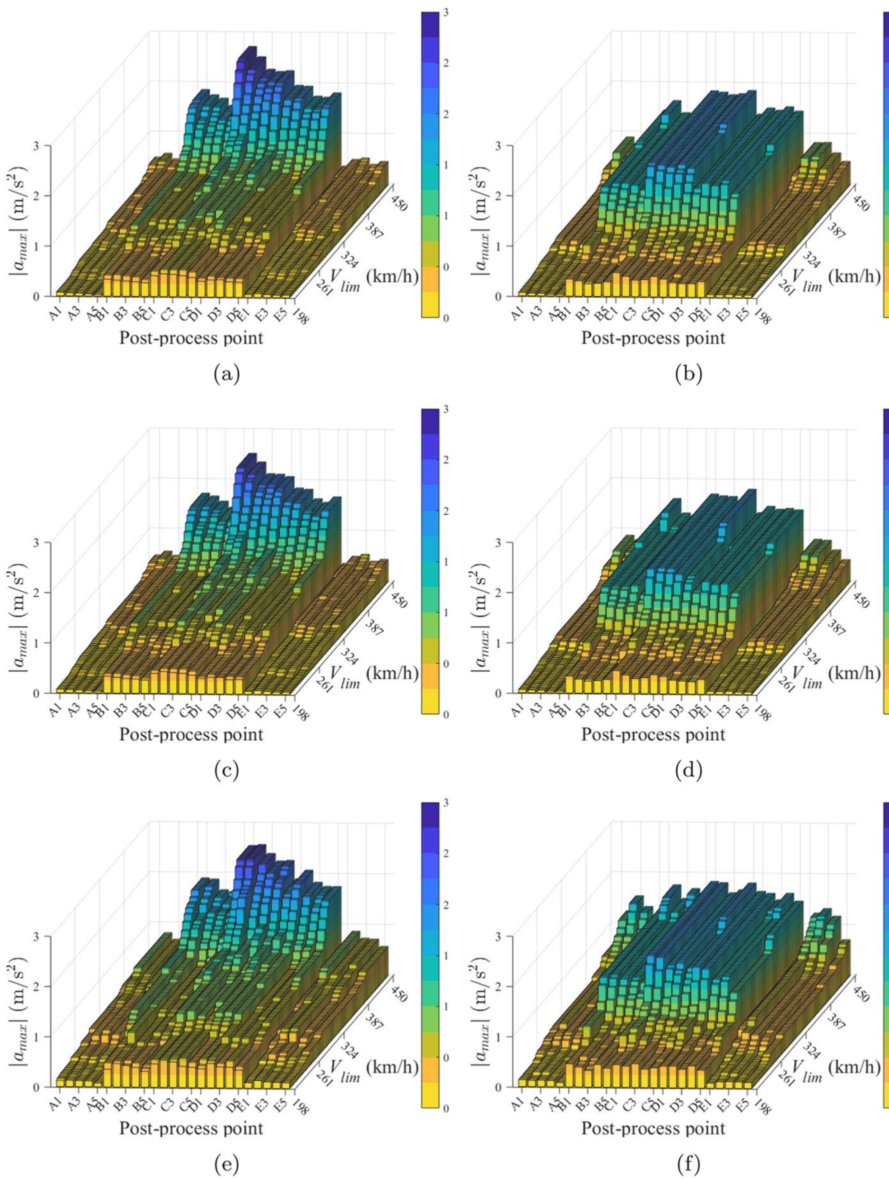

Fig. 12 Jabalón Bridge single-span β=134° model. Vertical acceleration under (**a**, **c**, **e**) S100 and (**b**, **d**, **f**) S102 trains. **a**, **b** for TLM excitacion model, **c**, **d** for VBI and **e**, **f** for VBI-η

extended, obtained using the TLM, VBI, and VBI-η excitation models, respectively. Figure 12b, d, f present the corresponding plots for RENFE S102.

As can be seen in Fig. 12a, c, e the circulation of the RENFE S100 induces an overall maximum response of the bridge at the mid-span external border (point C1). For a better interpretation of this result, Fig. 13a shows the maximum acceleration at C1 for each train speed. The distance between shared bogies of RENFE S100 is 18.7 m, a characteristic length that governs the most significant peaks in the bridge's vertical response. The first and second resonances of the fundamental longitudinal mode theoretically occur at $V^R_{1,1} = 408.6\,\mathrm{km/h}$ and $V^R_{1,2} = 204.3\,\mathrm{km/h}$, respectively, and are clearly visible in Fig. 13a. Additionally, the second resonance of the first torsional mode is excited by this train at $V^R_{2,2} = 266.98\,\mathrm{km/h}$, causing an increase in the response at the deck edges (points C1 and C5), as can be observed in Fig. 12a, c, e and in the peak around 267 km/h shown in Fig. 13a.

It is also worth noting that the second longitudinal bending frequency of the Jabalón Bridge single-span model is 17.97 Hz, still below the 30 Hz frequency limit, and is therefore included in the analysis. The third resonance of this mode is excited by RENFE S100 at $V^R_{X,3} = 403.16\,\mathrm{km/h}$ and explains the increase in response at the quarter- and three-quarter-span points (points B_i and D_i) at speeds of 400 km/h and above in Fig. 12a, c, e.

The circulation of RENFE S102 induces overall maximum responses at the mid-span border C5, according to Fig. 12b, d, f. Again, the evolution of the acceleration levels at the critical point C5 with the speed are presented in Fig. 13b. S102 is a conventional train with shared axles spaced 13.14 m apart. Due to this relatively short characteristic distance, typical of TALGO trains, resonances of the first modes are excited at much lower speeds. In particular, the first resonance of the fundamental mode occurs at approximately 287.1 km/h. Beyond this speed, only a slight amplification at the mid-span border (C5) is observed, resulting from the first resonance of the first torsional mode, which occurs near 375 km/h.

Finally, Fig. 14 depicts the envelopes of maximum acceleration for all post-processing points as a function of V_{lim} for both trains. Regarding the excitation models, vehicle-bridge interaction plays a minor role in both cases. Its effect is only noticeable at resonance and consistently results in lower deck accelerations. As for the influence of track

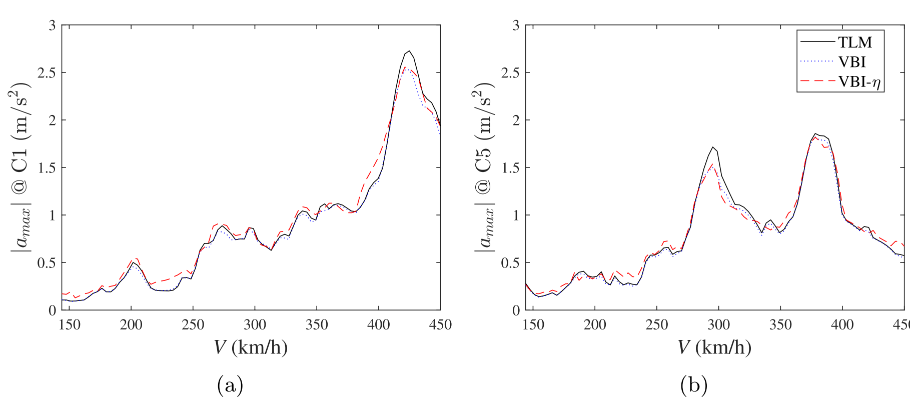

Fig. 13 Jabalón Bridge single-span span β=134° model. Vertical acceleration in the span edges vs. train speed (V) under (**a**) S100 and (**b**) S102 trains

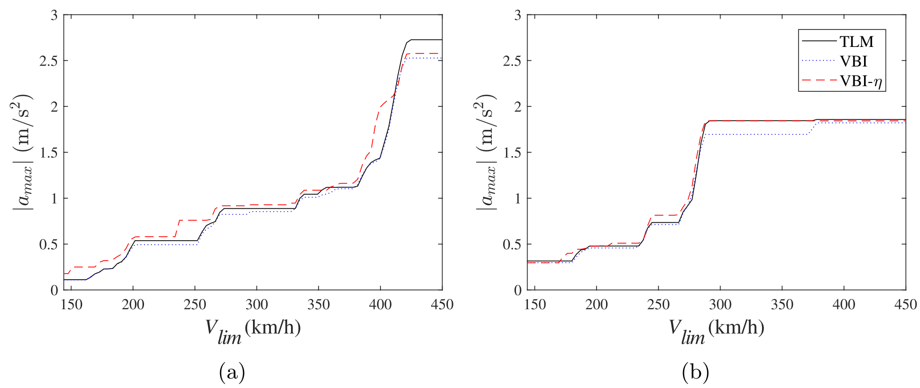

Fig. 14 Jabalón Bridge single-span β=134° model. Vertical acceleration envelopes vs. maximum train speed (V_{lim}) under (**a**) RENFE S100 and (**b**) RENFE S102 trains

irregularities, at moderate speeds, the response predicted by the VBI-η model slightly exceeds that of TLM; however, at the most prominent resonances, TLM predictions remain conservative for this particular track unevenness realization.

5.3 Influence of the weak span connection on the bridge vertical response

In this section, the train-induced vibrational response of the Jabalón Bridge is evaluated using the full three-span skewed calibrated model described in Sect. 3.1. Particular attention is given to the weak connection between the side spans and its influence on the deck's vertical acceleration. The spans are connected primarily through the continuous rails and the ballast, which is modeled as a transversely isotropic elastic material in the vicinity of the joints. In the following analysis, the degraded stiffness of the ballast connection is reduced relative to the calibrated or nominal values reported in Table 1. To this end, $E_{bX} = E_{bY}$ and E_{bZ}(hereafter E_{bD}) and $G_{bXY}, G_{bXZ} = G_{bYZ}$ (hereafter G_{bDD}) are progressively decreased.

Figure 15 shows the maximum vertical acceleration under the passage of the HSLM-A10 train at two points in each of the first (a)-(b), second (c)-(d), and third (e)-(f) spans. In the left-hand plots, two prominent peaks corresponding to the second and third resonances of the fundamental mode ($f_1 = 6.086$ Hz in the reference case) are observed near 295 km/h and 197 km/h. The first resonance of the fundamental mode is not reached with this train under 450 km/h due to its long characteristic distance ($d_k = 27$ m). In the right-hand plots, representing the deck edge, two additional peaks appear near 380 km/h and 250 km/h, associated with the second and third resonances of a torsional mode.

The response of the reference three-span model is shown as a continuous thick black line. The model is then modified by softening the degraded ballast properties, and the recalculated response is superimposed. The case with maximum material relaxation ($E_{bD}/25, G_{bDD}/25$) is plotted as a dashed black line.

It can be observed that the effect of softening the degraded ballast regions is very limited outside resonance. Resonant velocities shift slightly lower and the corresponding peaks move to the left due to reductions in the bending and torsion frequencies. Changes in peak amplitude at resonance do not always follow a consistent trend; this depends on the amplitude of free vibrations induced by individual axle loads as they exit the bridge for the particular mode and resonant speed. Figure 16

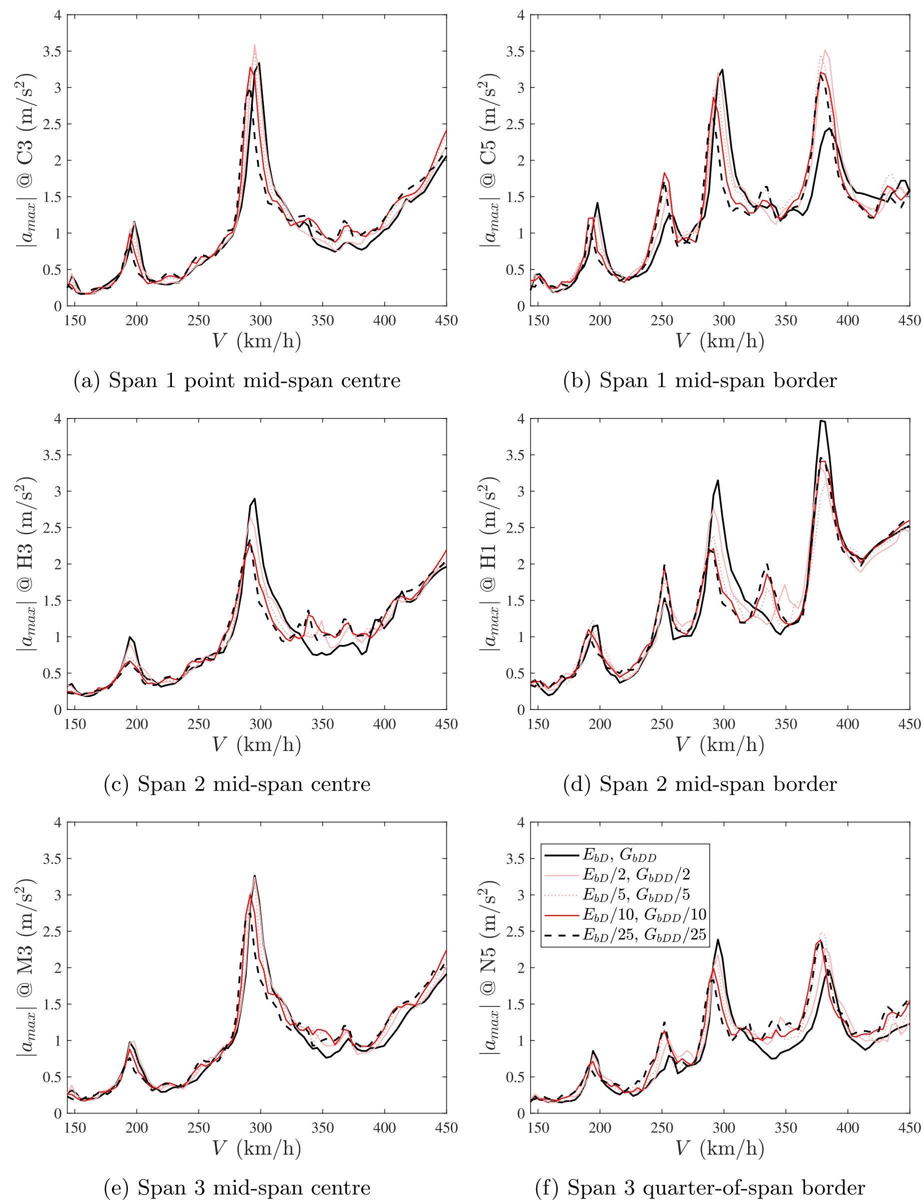

(a) Span 1 point mid-span centre (b) Span 1 mid-span border

(c) Span 2 mid-span centre (d) Span 2 mid-span border

(e) Span 3 mid-span centre (f) Span 3 quarter-of-span border

Fig. 15 Maximum acceleration in Jabalón Bridge complete under HLSM-A10 TLM train. Effect of reducing degraded ballast elastic properties. E_{bD} refers to the ballast elastic properties $E_{bX} = E_{bY}$ and E_{bZ}, while G_{bDD} to the ballast shear properties G_{bXY}, $G_{bXZ} = G_{bYZ}$

shows the overall maximum acceleration for the ten HSLM-A trains at the 75 post-processing points distributed over the three spans, as a function of the upper speed limit V_{lim}. Figure 16a corresponds to the original model, while Fig. 16b represents the model with the highest degree of span disconnection ($E_{bD}/25$, $G_{bDD}/25$). In general, the maximum response on the supports increases with relaxation of the elastic properties of the degraded ballast. However, away from the supports, as the connection between spans weakens, the response tends to increase in the first and third spans and decrease in the central span, particularly at higher speeds.

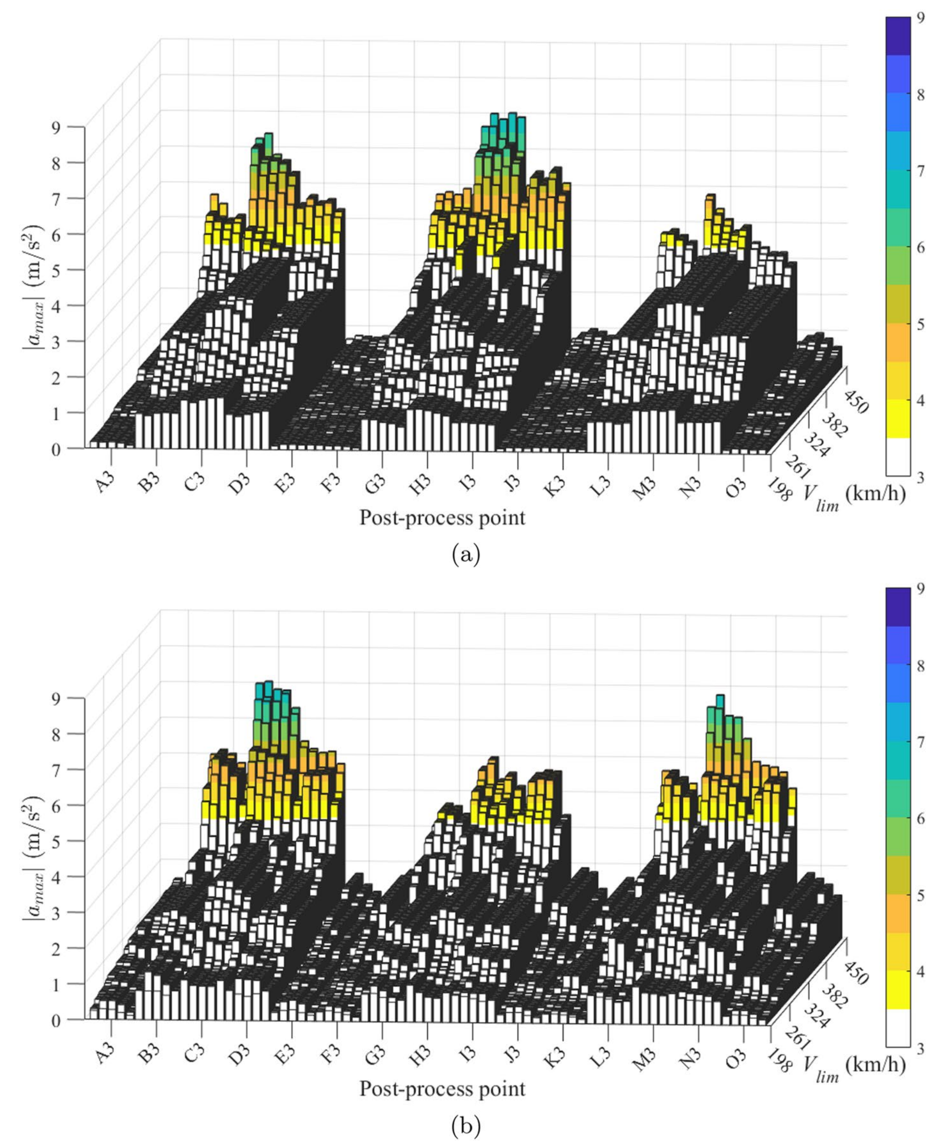

Fig. 16 Jabalón Bridge tree-span, β=134° model. Vertical acceleration under HSLM-A TLM trains. **a** Degraded ballast nominal properties: E_{bD}, G_{bDD}; **b** degraded ballast softened properties: $E_{bD}/25$, $G_{bDD}/25$

Finally, Fig. 17a, b, and c show the envelopes of maximum acceleration for all trains and all post-processing points as a function of V_{lim} in each of the three spans. In the central span, the overall maximum response is always predicted by the reference (nominal) model, with the stiffest connection to the exterior spans. For external spans, the model that produces the maximum acceleration depends on the speed window. Nevertheless, at higher speeds, the softer models yield the highest responses, consistent with the previous observations.

5.4 Bridge vertical acceleration prediction according to codes

In this section, the maximum bridge response predicted numerically using the 3D FE model in two of its variants is compared with the results of a normative analysis.

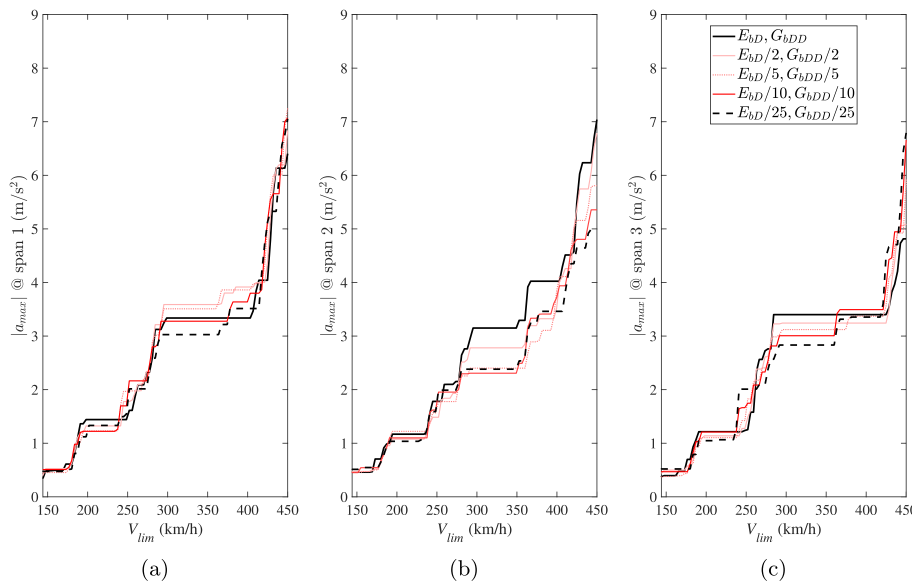

Fig. 17 Jabalón Bridge tree-span, β=134° model. Vertical acceleration envelopes at the (**a**) first, (**b**) second and (**c**) third span vs. V_{lim} under HSLM-A trains

Table 2 Jabalón Bridge first longitudinal bending (LB), first torsion (T) and first transverse bending (TB) frequencies: experimental identification, normative model and numerical 3D FE predictions

Jabalón Br. Mode	Experim. f_i (Hz)	EC1 Orth. plate f_i (Hz)	3D FE 134° single-sp f_i (Hz)	3D FE 134° tree-sp f_i (Hz)
LB	6.3	6.3	6.1	6.1
T	7.2	7.0	7.9	7.4
TB	9.3	9.5	10.4	9.9

According to Sect. 8.4.4 of Eurocode 1 (CEN 2023), due to the design speed and the pronounced deck skewness, an explicit dynamic analysis is required, considering the contribution of 3D modes. Accordingly, the bridge is also analyzed using a standard consultancy model, which is significantly less detailed than the one implemented in this study. The features of this simplified model are as follows: (i) only one deck, is represented as an orthotropic, skewed plate simply-supported along the end sections; (ii) model properties correspond to the nominal values derived from the project technical drawings; (iii) axle loads are distributed between two load lines along the rail axes; (iv) the track is not explicitly modeled, with its weight uniformly distributed over the ballast area; (v) axle loads are longitudinally distributed over three rail supports according to Sect. 8.3.6.2; and (vi) modal contributions up to 30 Hz are considered, with the prescribed normative damping being applied. The vertical response is again obtained through modal superposition of the normal modes, with the modal equations integrated in the time domain and the results post-processed at the same 25 points uniformly distributed over the platform area.

Table 2 presents the frequencies of the first longitudinal bending (LB), first torsional (T), and first transverse bending (TB) modes of the Jabalón Bridge, as experimentally identified and as predicted by the orthotropic plate model and the 3D FE skewed single-span and three-span models. It should be noted that in the latter model, multiple torsional modes appear within the frequency range [7.4–9] Hz.

Figure 18 shows the maximum acceleration envelope for the 25 post-processing points as the upper limit of the speed window, V_{lim}, is increased. Black, red, and blue lines correspond to the orthotropic plate normative model, the full 3D three-span skewed FE model, and the corresponding single-span FE model, respectively. In all cases, the response is computed under the circulation of HSLM-A trains. For both FE models, results for TLM and VBI-η excitation are provided.

In general, for any speed range, the code-based model is overly conservative, leading to predictions of cumulative acceleration close to twice those obtained with detailed models. The significance of this phenomenon increases as the maximum speed of interest rises, since the predicted acceleration levels are higher. In this regard, when a code-based model is applied, the analyzed structure would exceed the acceleration limit of 3.5 m/s^2 at approximately 270 km/h, whereas if the structure is analyzed using a detailed model, this threshold could increase up to 350 km/h. This phenomenon is closely related to the axle load distribution assumed in each case. The longitudinal load distribution per axle adopted in the code-based model (distributed over three sleepers) is much more severe than in the 3D track model, where a more realistic load distribution occurs due to the inclusion of the flexibility of the rail, rail pad, and ballast layer.

6 Conclusions

This study evaluates the SLS compliance of skewed multi-girder railway bridges with weakly connected spans under speed upgrading scenarios. By progressively extending the operational speed window, the research focuses specifically on the impact of deck skewness and the choice of railway excitation model. The SLS response depends on specific speed thresholds at which different physical mechanisms and modeling

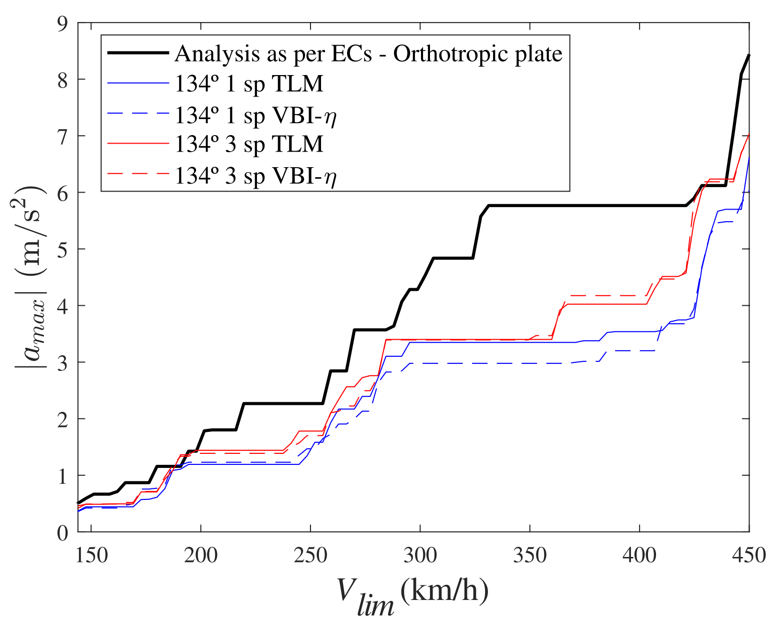

Fig. 18 Jabalón Bridge vertical acceleration envelopes vs. V_{lim} under HSLM-A trains. Full 3D three-span FE model and single-span orthotropic plate normative analyses

requirements become dominant. Based on the analysis, the following conclusions are drawn.

At very low speeds, no significant differences are observed in the bridge response between the three train models considered since the dynamic response is primarily quasi-static. As expected, the structure under study consistently fulfills SLS requirements since it is designed for high-speed. As speeds transition into the high-speed range (200–300 km/h), deck skewness emerges as a critical control factor and is beneficial for SLS compliance, since the maximum acceleration itself tends to decrease with skewness. This effect is partially related to the increase in natural frequencies as the deck becomes skewed, which raises the resonant speeds and, in some cases, moves potential resonance peaks outside the typical operational window for current rolling stock. In the particular bridge assessed in this study, increasing the skew angle from 90° to 134° raises the first longitudinal bending frequency from 5.75 Hz to 6.3 Hz and the first torsional frequency from 7.59 Hz to 7.93 Hz. Track irregularities become also a potential key factor, increasing the variability of the response. However, due to the stochastic nature of the track unevenness a rigorous statistical analysis would be necessary to accurately quantify its effects.

For very high-speed scenarios (exceeding 300 km/h), the assessment of SLS compliance becomes significantly more complex, and a series of key factors acquire particular relevance. VBI effects may have a more pronounce effect leading to lower structural responses. This is expected as lower-order resonances occur at higher velocities, and resonance-induced effects are more evident in these cases due to the absence of load-free cycles. Additionally, the uncertainties derived from the inclusion of track irregularities also play a role, entailing potential amplification margins on the maximum acceleration response when compared to perfect track conservation situations. Furthermore, the structural behavior is influenced by the weak coupling exerted by the ballast between spans and affects the spatial acceleration distribution across the bridge deck. The maximum structural response increases close to the span supports when the elastic properties of the ballast at span interfaces are relaxed. However, away from the supports, as the connection between spans weakens, the response tends to increase in the initial and final spans and decrease in the central span.

Finally, analyses conducted according to code provisions using a SS skewed orthotropic plate tend to overestimate the maximum acceleration, especially when the maximum speed of interest exceeds 300 km/h. This is partly related to the normative axle load distribution over three sleeper supports, which may be too conservative. Therefore, for advanced speed upgrading scenarios, simulating the axle load distribution of the ballast and the specific state of the track is recommended to ensure both safety and the rational use of infrastructure resources.

It is expected that the conclusions derived from this work are also applicable to other typologies with behavior comparable to that of an isotropic or orthotropic plate (solid and voided slabs, pseudo-slabs, etc.), in which the dynamic response is mainly governed by global deformation modes (longitudinal and transverse bending, torsion). Other typologies require a specific study that falls outside the scope of this work and may be of interest for future research.

Appendix

1 Train model parameters

Table 3 Axle loads an distances in the TLM model of trains HSLM-A, RENFE S100 and RENFE S102

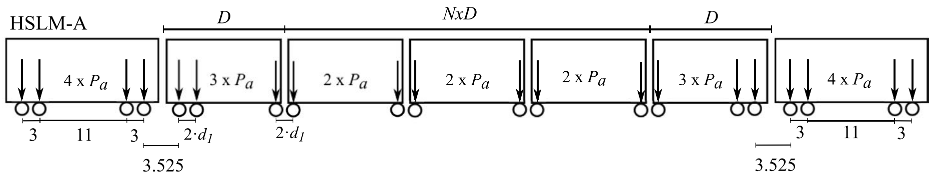

HSLM-A	A1	A2	A3	A4	A5	A6	A7	A8	A9	A10	Unit
N	18	17	16	15	14	13	13	12	11	11	-
D	18	19	20	21	22	23	24	25	26	27	m
$2 \cdot d_1$	2.00	3.50	2.00	3.00	2.00	2.00	2.00	2.50	2.00	2.00	m
$\mathrm{P_a}$	170	200	180	190	170	180	190	190	210	210	kN

S100

Axle	P_a (kN)	d_a (m)	Axle	P_a (kN)	d_a (m)	Axle	P_a (kN)	d_a (m)
1	170	3.78	10	135	64.18	19	135	154.68
2	170	6.78	11	221	79.88	20	135	157.68
3	170	17.78	12	221	82.88	21	84	173.27
4	170	20.78	13	221	98.58	22	84	176.27
5	84	23.88	14	221	101.58	23	170	179.37
6	84	26.88	15	135	117.28	24	170	182.37
7	135	42.48	16	135	120.28	25	170	193.37
8	135	45.48	17	135	135.98	26	170	196.37
9	135	61.18	18	135	138.98			

S102

Axle	P_a (kN)	d_a (m)	Axle	P_a (kN)	d_a (m)	Axle	P_a (kN)	d_a (m)
1	170	4.59	8	152	60.77	15	152	152.75
2	170	7.24	9	152	73.91	16	152	165.89
3	170	15.59	10	152	87.05	17	94	176.41
4	170	18.24	11	152	100.19	18	170	182.15
5	94	23.97	12	152	113.33	19	170	184.79
6	152	34.49	13	152	126.47	20	170	193.15
7	152	47.63	14	152	139.61	21	170	195.79

Table 4 VBI model parameters for the HSLM-A trains (suspension properties per spring-dashpot unit**)**

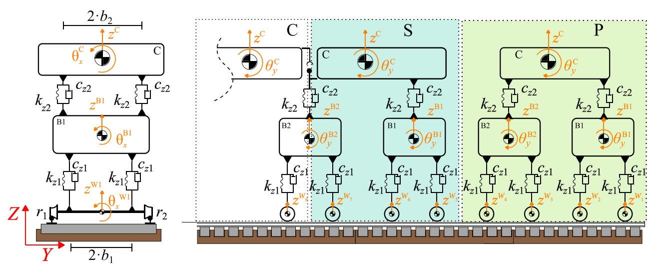

Vehicle	Notation	A1	A2	A3	A4	A5	Unit
C	m^C	27160	33280	29200	31240	27160	kg
	I_y^C	910	1410	1190	1510	1310	$\cdot 10^3 (\text{kg} \cdot \text{m}^2)$
	I_y^B	1240	3650	1240	2700	1240	$\text{kg} \cdot \text{m}^2$
S	m^C	40740	49910	43800	46850	40740	kg
	I_y^C	1020	1520	1370	1690	1540	$\cdot 10^3 (\text{kg} \cdot \text{m}^2)$
	I_y^B	1240	3650	1240	2700	1240	$\text{kg} \cdot \text{m}^2$
	$M_{adic,y}^C$	1014.9	1263.9	1234.3	1358.8	1281.3	$\text{kN} \cdot \text{m}$
P	m^C	54320	66550	58400	62470	54320	kg
	I_y^C	1330	1620	1430	1530	1330	$\cdot 10^3 (\text{kg} \cdot \text{m}^2)$
	I_y^B	2700	2700	2700	2700	2700	$\text{kg} \cdot \text{m}^2$
P,	k_{z1}	705	660	690	675	6705	kN/m
S	c_{z1}	10	9.5	10	9.5	10	$\text{kN} \cdot \text{s/m}$
and	k_{z2}	320	410	350	380	320	kN/m
C	c_{z2}	19.5	25	21.5	23	19.5	$\text{kN} \cdot \text{s/m}$

Vehicle	Notation	A6	A7	A8	A9	A10	Unit
C	m^C	29200	31240	31240	35310	35310	kg
	I_y^C	1530	1770	1980	2320	2490	$\cdot 10^3 (\text{kg} \cdot \text{m}^2)$
	I_y^B	1240	1240	1900	1240	1240	$\text{kg} \cdot \text{m}^2$
S	m^C	43800	46850	46850	52970	52970	kg
	I_y^C	1820	2120	2360	2830	3060	$\cdot 10^3 (\text{kg} \cdot \text{m}^2)$
	I_y^B	1240	1240	1900	1240	1240	$\text{kg} \cdot \text{m}^2$
	$M_{adic,y}^C$	1449.1	1626.9	1684.4	2012.5	2099.1	$\text{kN} \cdot \text{m}$
P	m^C	58400	62470	62470	70630	70630	kg
	I_y^C	1430	1530	1530	1720	1720	$\cdot 10^3 (\text{kg} \cdot \text{m}^2)$
	I_y^B	2700	2700	2700	2700	2700	$\text{kg} \cdot \text{m}^2$
P,	k_{z1}	690	675	675	640	640	kN/m
S	c_{z1}	10	9.5	9.5	9.5	9.5	$\text{kN} \cdot \text{s/m}$
and	k_{z2}	350	380	380	440	440	kN/m
C	c_{z2}	21.5	23	23	26.5	26.5	$\text{kN} \cdot \text{s/m}$

Notation	b_1	b_2	g	I_x^C	m^B	I_x^B	m^W	I_x^W
Value	0.7175	1.085	-9.81	119328	3500	2835	2000	1000
Unit	m	m	m/s^2	$\text{kg} \cdot \text{m}^2$	kg	$\text{kg} \cdot \text{m}^2$	kg	$\text{kg} \cdot \text{m}^2$

Table 5 VBI model parameters for RENFE S102 and RENFE S100 trains (suspension properties per spring–dashpot unit)

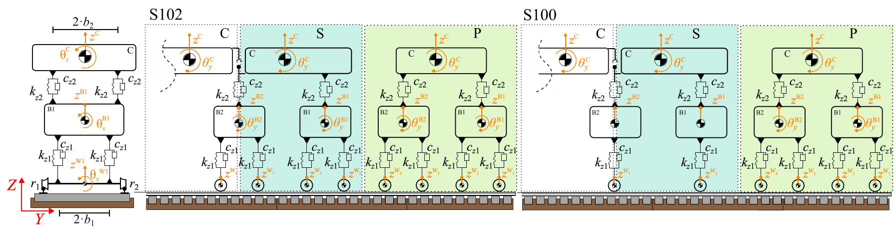

Notation	S102 P	S102 S	S102 C	S100 P	S100 S	S100 C	Unit
b_1	0.718	0.718	0.718	0.718	0.718	0.718	m
b_2	1.099	0.718	0.718	1.085	1.085	1.085	m
m^C	53200	11658	11658	54988	26147	24000	kg
I_x^C	78743	13843	13843	59478	33982	31186	$\mathrm{kg \cdot m^2}$
I_y^C	1813233	173173	173173	1133384	1005092	893038	$\mathrm{kg \cdot m^2}$
k_{z2}	$597 \cdot 10^3$	$165.6 \cdot 10^3$	$165.6 \cdot 10^3$	$1225 \cdot 10^3$	$410 \cdot 10^3$	$410 \cdot 10^3$	N/m
c_{z2}	$100 \cdot 10^3$	$12 \cdot 10^3$	$12 \cdot 10^3$	$20 \cdot 10^3$	$24 \cdot 10^3$	$24 \cdot 10^3$	$\mathrm{N \cdot s/m}$
m^B	3600	1757	1757	3040	3040	3040	kg
I_x^B	2421	2199	2199	2045	2045	2045	$\mathrm{kg \cdot m^2}$
I_y^B	3816	2044	2044	3223	3223	3223	$\mathrm{kg \cdot m^2}$
k_{z1}	$984.7 \cdot 10^3$	$679.2 \cdot 10^3$	$679.2 \cdot 10^3$	$1200 \cdot 10^3$	$700 \cdot 10^3$	$700 \cdot 10^3$	N/m
c_{z1}	$26 \cdot 10^3$	$8.4 \cdot 10^3$	$8.4 \cdot 10^3$	$10 \cdot 10^3$	$5 \cdot 10^3$	$5 \cdot 10^3$	$\mathrm{N \cdot s/m}$
m^W	1900	1789	1789	1733	1830	1830	kg
I_x^W	956	900	900	872	896	896	$\mathrm{kg \cdot m^2}$

2 Train matrices

In the following, the matrices of the articulated and regular trains that define Eq. 5 are presented. All trains consist of two power cars and n passenger carriages, arranged as $n-2$ central cars and two side cars (see Fig. 19). The spacing between shared bogies is constant for all central carriages and is denoted as $2 \cdot d_2$, allowing for a more compact formulation. In the side cars, the distance between the independent bogie and the first shared bogie is $2 \cdot d_S$. For convenience, the passenger carriages are assigned a compact numbering scheme in the matrix equations, from A_1 to A_n, with A_1 representing the first side car and A_n the last one.

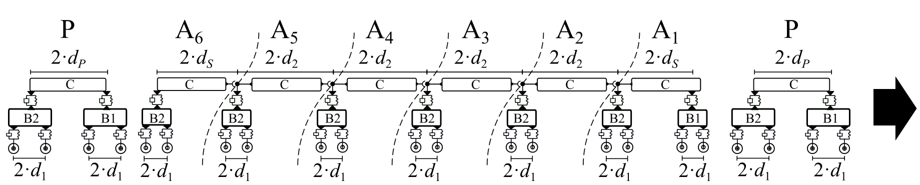

Fig. 19 Articulated train composed by 11 bogies and 6 articulated carriages: 2 power-cars, 2 side-cars and 4 central-cars

Due to the presence of the hinge between passenger cars, the vertical displacement z^{C} of all the $n-1$ car bodies in the passenger carriages are dependent DOFs, which are related to those of the first side car (vehicle A_1) and to the pitching movements θ_y^{C} of the preceding vehicles as follows:

$$z^{C}_{\mathrm{A}_i} = \begin{cases} z^{\mathrm{C}}_{\mathrm{A}_1} + d_S \cdot \theta^{\mathrm{C}}_{y,\mathrm{A}_1} + \sum_{j=2}^{i-1}\left[2d_2 \cdot \theta^{\mathrm{C}}_{y,\mathrm{A}_j}\right] + d_2 \cdot \theta^{\mathrm{C}}_{y,\mathrm{A}_i} & 2 \leq i < n \\ z^{\mathrm{C}}_{\mathrm{A}_1} + d_S \cdot \theta^{\mathrm{C}}_{y,\mathrm{A}_1} + \sum_{j=2}^{n-1}\left[2d_2 \cdot \theta^{\mathrm{C}}_{y,\mathrm{A}_j}\right] + d_S \cdot \theta^{\mathrm{C}}_{y,\mathrm{A}_n} & i = n \end{cases} \tag{14}$$

Therefore, the vector that contains the independent DOFs of the car bodies and bogies of the articulated trains, $\mathbf{x}_v$, is

$$\mathbf{x}_v = \mathrm{column}\left[\boldsymbol{x}^{P} \quad \boldsymbol{x}^{A1} \quad \ldots \quad \boldsymbol{x}^{Ai} \quad \ldots \quad \boldsymbol{x}^{An} \quad \boldsymbol{x}^{P}\right] \tag{15}$$

$\boldsymbol{x}^{P}$, $\boldsymbol{x}^{A1}$ and $\boldsymbol{x}^{Ai}$ refer to the independent DOFs that belong to the power car, first side car and the remaining side cars, respectively. Therefore, they are defined as provided in what follows:

$$\boldsymbol{x}^{P} = \left[z^{\mathrm{C}}_{\mathrm{P}} \quad \theta^{\mathrm{C}}_{x,\mathrm{P}} \quad \theta^{\mathrm{C}}_{y,\mathrm{P}} \quad z^{\mathrm{B1}}_{\mathrm{P}} \quad \theta^{\mathrm{B1}}_{x,\mathrm{P}} \quad \theta^{\mathrm{B1}}_{y,\mathrm{P}} \quad z^{\mathrm{B2}}_{\mathrm{P}} \quad \theta^{\mathrm{B2}}_{x,\mathrm{P}} \quad \theta^{\mathrm{B2}}_{y,\mathrm{P}}\right]^{\mathrm{T}} \tag{16}$$

$$\boldsymbol{x}^{A1} = \left[z^{\mathrm{C}}_{\mathrm{A}_1} \quad \theta^{\mathrm{C}}_{x,\mathrm{A}_1} \quad \theta^{\mathrm{C}}_{y,\mathrm{A}_1} \quad z^{\mathrm{B1}}_{\mathrm{A}_1} \quad \theta^{\mathrm{B1}}_{x,\mathrm{A}_1} \quad \theta^{\mathrm{B1}}_{y,\mathrm{A}_1} \quad z^{\mathrm{B2}}_{\mathrm{A}_1} \quad \theta^{\mathrm{B2}}_{x,\mathrm{A}_1} \quad \theta^{\mathrm{B2}}_{y,\mathrm{A}_1}\right]^{\mathrm{T}} \tag{17}$$

$$\boldsymbol{x}^{Ai} = \left[\theta^{\mathrm{C}}_{x,\mathrm{A}_i} \quad \theta^{\mathrm{C}}_{y,\mathrm{A}_i} \quad z^{\mathrm{B2}}_{\mathrm{A}_i} \quad \theta^{\mathrm{B2}}_{x,\mathrm{A}_i} \quad \theta^{\mathrm{B2}}_{y,\mathrm{A}_i}\right]^{\mathrm{T}} \quad i \neq 1 \tag{18}$$

In Eqs. 14, 16, 17, 18, the DOFs associated to vertical displacements of carbodies and bogies (z^{C} and z^{Bi}, respectively), rolling (θ^{C}_x and θ^{Bi}_x), and pitching (θ^{C}_y and θ^{Bi}_y) are accompanied by an additional subindex $x = P, A_1, A_i$, which refers to the type of vehicle (power, first side car and remaining side cars). This additional subindex is also used throughout this appendix to refer the suspension properties of the trains provided in Tables 4 and 5.

The vector that contains the DOFs of the wheelsets $\mathbf{x}_w$ is defined as

$$\mathbf{x}_w = \mathrm{column}\left[\boldsymbol{x}^{W_1} \quad \boldsymbol{x}^{W_2} \quad \ldots \quad \boldsymbol{x}^{W_i} \quad \ldots \quad \boldsymbol{x}^{W_{Nw}}\right], \quad \boldsymbol{x}_{W_i} = \left[z^{\mathrm{W}_i} \quad \theta^{\mathrm{W}_i}_x\right]^{\mathrm{T}} \tag{19}$$

For regular trains, the DOFs associated to pitching movements of the bogies in the passenger carriages, θ^{B1}_y and θ^{B2}_y, vanish in Eqs. 17 and 18.

The mass matrix $\mathbf{M}_v$ of Eq. 5 for articulated trains is presented in Eq. 20, and its submatrices are depicted in equations Eqs. 21 to 26.

$$\mathbf{M}_v = \mathrm{diag}\left[\boldsymbol{M}^{P}_{v} \quad \boldsymbol{M}^{A}_{v} \quad \boldsymbol{M}^{P}_{v}\right] \tag{20}$$

$$\begin{aligned} \boldsymbol{M}^{P}_{v} &= \mathrm{diag}\left[\boldsymbol{M}^{P}_{C} \quad \boldsymbol{M}^{P}_{B} \quad \boldsymbol{M}^{P}_{B}\right] \\ \boldsymbol{M}^{P}_{C} &= \mathrm{diag}\left[m^{C}_{\mathrm{P}} \quad I^{C}_{x,\mathrm{P}} \quad I^{C}_{y,\mathrm{P}}\right] \quad \boldsymbol{M}^{P}_{B} = \mathrm{diag}\left[m^{B}_{\mathrm{P}} \quad I^{B}_{x,\mathrm{P}} \quad I^{B}_{y,\mathrm{P}}\right] \end{aligned} \tag{21}$$

$$\boldsymbol{M}^{A}_{v} = \begin{bmatrix} \boldsymbol{M}^{A1,A1}_{v} & & & & & sym. \\ \boldsymbol{M}^{A2,A1}_{v} & \boldsymbol{M}^{A2,A2}_{v} & & & & \\ \vdots & \vdots & \ddots & & & \\ \boldsymbol{M}^{Ai,A1}_{v} & \boldsymbol{M}^{Ai,A2}_{v} & \ldots & \boldsymbol{M}^{Ai,Ai}_{v} & & \\ \vdots & \vdots & & \vdots & \ddots & \\ \boldsymbol{M}^{An,A1}_{v} & \boldsymbol{M}^{An,A2}_{v} & \ldots & \boldsymbol{M}^{An,Ai}_{v} & \ldots & \boldsymbol{M}^{An,An}_{v} \end{bmatrix} \tag{22}$$

$$
\begin{aligned}
\boldsymbol{M}_{\boldsymbol{v}}^{\boldsymbol{A1},\boldsymbol{A1}} &= \mathrm{diag}\left[\, \boldsymbol{M}_{\boldsymbol{C}}^{\boldsymbol{A1}} \quad \boldsymbol{M}_{\boldsymbol{B}}^{\boldsymbol{A1}} \quad \boldsymbol{M}_{\boldsymbol{B}}^{\boldsymbol{A1}} \,\right] \\
\boldsymbol{M}_{\boldsymbol{C}}^{\boldsymbol{A1}} &= \begin{bmatrix} \sum_{i=1}^{n} m_{\mathrm{A}_i}^{C} & & sym. \\ 0 & I_{x,\mathrm{A}_1}^{C} & \\ d_S \sum_{i=2}^{n} m_{\mathrm{A}_i}^{C} & 0 & I_{y,\mathrm{A}_1}^{C} + d_S^2 \sum_{i=2}^{n} m_{\mathrm{A}_i}^{C} \end{bmatrix} \\
\boldsymbol{M}_{\boldsymbol{B}}^{\boldsymbol{A1}} &= \mathrm{diag}\left[\, m_{\mathrm{A}_1}^{B} \quad I_{x,\mathrm{A}_1}^{B} \quad I_{y,\mathrm{A}_1}^{B} \,\right]
\end{aligned}
\tag{23}
$$

$$
\begin{aligned}
& i \neq 1 \\
\boldsymbol{M}_{\boldsymbol{v}}{}^{\boldsymbol{Ai},\boldsymbol{Ai}} &= \mathrm{diag}\left[\, \boldsymbol{M}_{\boldsymbol{C}}^{\boldsymbol{Ai}} \quad \boldsymbol{M}_{\boldsymbol{B}}^{\boldsymbol{Ai}} \,\right] \\
\boldsymbol{M}_{\boldsymbol{C}}^{\boldsymbol{Ai}} &= \mathrm{diag}\left[\, I_{x,\mathrm{A}_i}^{C} \quad M_{C(2,2)}^{Ai} \,\right] \quad \boldsymbol{M}_{\boldsymbol{B}}^{\boldsymbol{Ai}} = \mathrm{diag}\left[\, m_{\mathrm{A}_i}^{B} \quad I_{x,\mathrm{A}_i}^{B} \quad I_{y,\mathrm{A}_i}^{B} \,\right] \\
M_{C(2,2)}^{Ai} &= \begin{cases} I_{y,\mathrm{A}_i}^{C} + d_2^2 m_{\mathrm{A}_i}^{C} + 4 d_2^2 \sum_{j=i+1}^{n} m_{\mathrm{A}_j}^{C} & i < n \\ I_{y,\mathrm{A}_n}^{C} + d_S^2 m_{\mathrm{A}_n}^{C} & i = n \end{cases}
\end{aligned}
\tag{24}
$$

$$
\begin{aligned}
& i \neq 1 \\
\boldsymbol{M}_{\boldsymbol{v}}{}^{\boldsymbol{A1},\boldsymbol{Ai}} &= \mathrm{diag}\left[\, \boldsymbol{M}_{\boldsymbol{C}}^{\boldsymbol{A1},\boldsymbol{Ai}} \quad [\mathbf{0}^{\boldsymbol{B}} \quad \mathbf{0}^{\boldsymbol{B}}]^{\mathrm{T}} \,\right] \\
\boldsymbol{M}_{\boldsymbol{C}}^{\boldsymbol{A1},\boldsymbol{Ai}} &= \begin{bmatrix} 0 & M_{C(1,2)}^{A1,Ai} \\ 0 & 0 \\ 0 & ds \cdot M_{C(1,2)}^{A1,Ai} \end{bmatrix} \quad \mathbf{0}^{\boldsymbol{B}} = \mathbf{0}_{3\times 3} \\
M_{C(1,2)}^{A1,Ai} &= \begin{cases} d_2 m_{\mathrm{A}_i}^{C} + 2 d_2 \sum_{j=i+1}^{n} m_{\mathrm{A}_j}^{C} & i < n \\ d_S m_{\mathrm{A}_n}^{C} & i = n \end{cases}
\end{aligned}
\tag{25}
$$

$$
\begin{aligned}
& i \neq 1 \quad \wedge \quad j > i \\
\boldsymbol{M}_{\boldsymbol{v}}^{\boldsymbol{Ai},\boldsymbol{Aj}} &= \mathrm{diag}\left[\, \boldsymbol{M}_{\boldsymbol{C}}^{\boldsymbol{Ai},\boldsymbol{Aj}} \quad \mathbf{0}^{\boldsymbol{B}} \,\right] \\
\boldsymbol{M}_{\boldsymbol{C}}^{\boldsymbol{Ai},\boldsymbol{Aj}} &= \begin{bmatrix} 0 & 0 \\ 0 & M_{C(2,2)}^{Ai,Aj} \end{bmatrix} \quad M_{C(2,2)}^{Ai,Aj} = \begin{cases} 2 d_2^2 m_{\mathrm{A}_j}^{C} + 4 d_2^2 \sum_{k=j+1}^{n} m_{\mathrm{A}_k}^{C} & j < n \\ 2 d_2 d_S m_{\mathrm{A}_n}^{C} & j = n \end{cases}
\end{aligned}
\tag{26}
$$

For regular trains, due to the absence of the pitching DOFs in the bogies of the passenger carriages (θ_y^{B1} and θ_y^{B2}), the mass matrix $\boldsymbol{M}_{\boldsymbol{v}}^{\boldsymbol{A}}$ shown in Eq. 22 must be modified removing the columns associated with the aforementioned DOFs as well as the corresponding rows.

The mass matrix $\mathbf{M}_w$ of Eq. 5 is described in what follows (Eq. 27), where N_w is the number of wheelsets of the train. This expression is valid for both articulated and regular trains.

$$
\mathbf{M}_w = \mathrm{diag}\left[\, \boldsymbol{M}_{\boldsymbol{w}_1} \quad \ldots \quad \boldsymbol{M}_{\boldsymbol{w}_i} \quad \ldots \quad \boldsymbol{M}_{\boldsymbol{w}_{Nw}} \,\right], \quad \boldsymbol{M}_{\boldsymbol{w}_i} = \begin{bmatrix} m^{Wi} & 0 \\ 0 & I_x^{Wi} \end{bmatrix}
\tag{27}
$$

The stiffness matrix $\mathbf{K}_v$ of articulated trains is presented in Eqs. 28 to 34.

$$
\mathbf{K}_v = \mathrm{diag}\left[\, \boldsymbol{K}_{\boldsymbol{v}}^{\boldsymbol{P}} \quad \boldsymbol{K}_{\boldsymbol{v}}^{\boldsymbol{A}} \quad \boldsymbol{K}_{\boldsymbol{v}}^{\boldsymbol{P}} \,\right]
\tag{28}
$$

$$
\boldsymbol{K_v^P} = \begin{bmatrix} \boldsymbol{K_C^P} & & sym. \\ \boldsymbol{K_{C,B1}^P} & \boldsymbol{K_{B1}^P} & \\ \boldsymbol{K_{C,B2}^P} & \boldsymbol{0} & \boldsymbol{K_{B2}^P} \end{bmatrix} \quad \boldsymbol{K_C^P} = \begin{bmatrix} 4k_{z2,\mathrm{P}} & & sym. \\ 0 & 4k_{z2,\mathrm{P}} \cdot {b_{2,\mathrm{P}}}^2 & \\ 0 & 0 & d_P^2 4k_{z2,\mathrm{P}} \end{bmatrix}
$$

$$
\boldsymbol{K_{B1}^P} = \boldsymbol{K_{B2}^P} = \begin{bmatrix} \begin{matrix} 2k_{z2,\mathrm{P}} \\ +4k_{z1,\mathrm{P}} \end{matrix} & & sym. \\ 0 & \begin{matrix} 2k_{z2,\mathrm{P}} \cdot b_{2,\mathrm{P}}^2 \\ +4k_{z1,\mathrm{P}} \cdot b_{1,\mathrm{P}}^2 \end{matrix} & \\ 0 & 0 & 4k_{z1,\mathrm{P}} \cdot d_{1,\mathrm{P}}^2 \end{bmatrix} \tag{29}
$$

$$
\boldsymbol{K_{C,Bj}^P} = \begin{bmatrix} -2k_{z2,\mathrm{P}} & 0 & -(-1)^j d_\mathrm{P} 2k_{z2,\mathrm{P}} \\ 0 & -2k_{z2,\mathrm{P}} \cdot b_{2,\mathrm{P}}^2 & 0 \\ 0 & 0 & 0 \end{bmatrix} \quad j = \{1,2\}
$$

$$
\boldsymbol{K_v^A} = \begin{bmatrix} \boldsymbol{K_v^{A1,A1}} & & & & & sym. \\ \boldsymbol{K_v^{A2,A1}} & \boldsymbol{K_v^{A2,A2}} & & & & \\ \vdots & \vdots & \ddots & & & \\ \boldsymbol{K_v^{Ai,A1}} & \boldsymbol{K_v^{Ai,A2}} & \ldots & \boldsymbol{K_v^{Ai,Ai}} & & \\ \vdots & \vdots & & \vdots & \ddots & \\ \boldsymbol{K_v^{An,A1}} & \boldsymbol{K_v^{An,A2}} & \ldots & \boldsymbol{K_v^{An,Ai}} & \ldots & \boldsymbol{K_v^{An,An}} \end{bmatrix} \tag{30}
$$

$$
\boldsymbol{K_v}^{\boldsymbol{A1,A1}} = \begin{bmatrix} \boldsymbol{K_C^{A1,A1}} & & sym. \\ \boldsymbol{K_{C,B1}^{A1,A1}} & \boldsymbol{K_{B1}^{A1,A1}} & \\ \boldsymbol{K_{C,B2}^{A1,A1}} & \boldsymbol{0} & \boldsymbol{K_{B2}^{A1,A1}} \end{bmatrix}
$$

$$
\boldsymbol{K_C^{A1,A1}} = \begin{bmatrix} \begin{matrix} 4k_{z2,\mathrm{A}_1} \\ +\sum_{j=2}^{n} 2k_{z2,\mathrm{A}_j} \end{matrix} & & sym. \\ 0 & 4k_{z2,\mathrm{A}_1} \cdot {b_{2,\mathrm{A}_1}}^2 & \\ d_S \sum_{j=2}^{n} 2k_{z2,\mathrm{A}_j} & 0 & \begin{matrix} d_S^2 4k_{z2,\mathrm{A}_1} \\ +d_S^2 \sum_{j=2}^{n} 2k_{z2,\mathrm{A}_j} \end{matrix} \end{bmatrix}
$$

$$
\boldsymbol{K_{B1}^{A1,A1}} = \boldsymbol{K_{B2}^{A1,A1}} = \begin{bmatrix} \begin{matrix} 2k_{z2,\mathrm{A}_1} \\ +4k_{z1,\mathrm{A}_1} \end{matrix} & & sym. \\ 0 & \begin{matrix} 2k_{z2,\mathrm{A}_1} \cdot b_{2,\mathrm{A}_1}^2 \\ +4k_{z1,\mathrm{A}_1} \cdot b_{1,\mathrm{A}_1}^2 \end{matrix} & \\ 0 & 0 & 4k_{z1,\mathrm{A}_1} \cdot d_{1,\mathrm{A}_1}^2 \end{bmatrix} \tag{31}
$$

$$
\boldsymbol{K_{C,Bj}^{A1,A1}} = \begin{bmatrix} -2k_{z2,\mathrm{A}_1} & 0 & -(-1)^j d_S 2k_{z2,\mathrm{A}_1} \\ 0 & -2k_{z2,\mathrm{A}_1} \cdot b_{2,\mathrm{A}_1}^2 & 0 \\ 0 & 0 & 0 \end{bmatrix} \quad j = \{1,2\}
$$

$i \neq 1$

$$
\boldsymbol{K_v^{Ai,Ai}} = \begin{bmatrix} 2k_{z2,\mathrm{A}_i} \cdot b_{2,\mathrm{A}_i}^2 & & & & sym. \\ 0 & K_{v(2,2)}^{Ai,Ai} & & & \\ 0 & K_{v(3,2)}^{Ai,Ai} & \begin{matrix} 2k_{z2,\mathrm{A}_i} \\ +4k_{z1,\mathrm{A}_i} \end{matrix} & & \\ -2k_{z2,\mathrm{A}_i} \cdot b_{2,\mathrm{A}_i}^2 & 0 & 0 & \begin{matrix} 2k_{z2,\mathrm{A}_i} \cdot b_{2,\mathrm{A}_i}^2 \\ +4k_{z1,\mathrm{A}_i} \cdot b_{1,\mathrm{A}_i}^2 \end{matrix} & \\ 0 & 0 & 0 & 0 & 4k_{z1,\mathrm{A}_i} \end{bmatrix} \tag{32}
$$

$$
K_{v(2,2)}^{Ai,Ai} = \begin{cases} 4d_2^2 \sum_i^n 2k_{z2,\mathrm{A}_i} & i < n \\ 4d_S^2 2k_{z2,\mathrm{A}_n} & i = n \end{cases} \quad K_{v(3,2)}^{Ai,Ai} = \begin{cases} -4d_2 k_{z2,\mathrm{A}_i} & i < n \\ -4d_S k_{z2,\mathrm{A}_n} & i = n \end{cases}
$$

$$
\begin{gathered}
i \neq 1 \\
\boldsymbol{K}_{\boldsymbol{v}}^{\boldsymbol{A1,Ai}} = \begin{bmatrix} \boldsymbol{K}_{\boldsymbol{C}}^{\boldsymbol{A1,Ai}} & \boldsymbol{0}^{\boldsymbol{K}} \end{bmatrix}^{\mathrm{T}} \\
\boldsymbol{K}_{\boldsymbol{C}}^{\boldsymbol{A1,Ai}} = \begin{bmatrix} 0 & 0 & 0 & 0 \\ K_{C(2,1)}^{A1,Ai} & 0 & K_{C(2,2)}^{A1,Ai} & 0 \\ -2k_{z2,\mathrm{A}_i} & 0 & -d_S 2k_{z2,\mathrm{A}_i} & 0 \\ 0 & 0 & 0 & 0 \\ 0 & 0 & 0 & 0 \end{bmatrix} \quad \boldsymbol{0}^{\boldsymbol{K}} = \boldsymbol{0}_{5\times 5} \\
K_{C(2,1)}^{A1,Ai} = \begin{cases} 2d_2 \sum_i^n 2k_{z2,\mathrm{A}_i} & i < n \\ 2d_S 2k_{z2,\mathrm{A}_n} & i = n \end{cases} \quad K_{C(2,2)}^{A1,Ai} = \begin{cases} 2d_2 d_S \sum_i^n 2k_{z2,\mathrm{A}_i} & i < n \\ 2d_S^2 2k_{z2,\mathrm{A}_n} & i = n \end{cases}
\end{gathered}
\tag{33}
$$

$$
\begin{gathered}
i \neq 1 \quad \wedge \quad j > i \\
\boldsymbol{K}_{\boldsymbol{v}}^{\boldsymbol{Ai,Aj}} = \begin{bmatrix} 0 & 0 & 0 & 0 & 0 \\ 0 & K_{v(2,2)}^{Ai,Aj} & -4d_2 k_{z2,\mathrm{A}_j} & 0 & 0 \\ 0 & 0 & 0 & 0 & 0 \\ 0 & 0 & 0 & 0 & 0 \\ 0 & 0 & 0 & 0 & 0 \end{bmatrix} \quad K_{v(2,2)}^{Ai,Aj} = \begin{cases} 4d_2^2 \sum_j^n 2k_{z2,\mathrm{A}_j} & j < n. \\ 4d_2 d_S 2k_{z2,\mathrm{A}_n} & j = n. \end{cases}
\end{gathered}
\tag{34}
$$

Again, for regular trains, due to the absence of pitching DOFs in the bogies of the passenger carriages, the stiffness matrix $\boldsymbol{K}_{\boldsymbol{v}}^{\boldsymbol{A}}$ shown in Eq. 30 must be modified removing the columns associated with the aforementioned DOFs as well as the corresponding rows. Furthermore, due to the presence of only one wheelset per bogie instead of two as in the articulated compositions, in matrices $\boldsymbol{K}_{\boldsymbol{Bj}}^{\boldsymbol{A1,A1}}$ (Eq. 31) and $\boldsymbol{K}_{\boldsymbol{v}}^{\boldsymbol{Ai,Ai}}$ (Eq. 32) parameter k_{z1} should be divided by 2.

$\mathbf{K}_{vw}$ matrix is described in Eqs. 35 to 38.

$$
\mathbf{K}_{vw} = \mathrm{diag}\begin{bmatrix} \boldsymbol{K}_{\boldsymbol{vw}}^{\boldsymbol{P}} & \boldsymbol{K}_{\boldsymbol{vw}}^{\boldsymbol{A1}} & \ldots & \boldsymbol{K}_{\boldsymbol{vw}}^{\boldsymbol{Ai}} & \ldots & \boldsymbol{K}_{\boldsymbol{vw}}^{\boldsymbol{An}} & \boldsymbol{K}_{\boldsymbol{vw}}^{\boldsymbol{P}} \end{bmatrix}
\tag{35}
$$

$$
\begin{gathered}
\boldsymbol{K}_{\boldsymbol{vw}}^{\boldsymbol{P}} = \begin{bmatrix} \boldsymbol{0}_{\boldsymbol{C}} & \mathrm{diag}[\boldsymbol{K}_{\boldsymbol{WB}}^{\boldsymbol{P}} \quad \boldsymbol{K}_{\boldsymbol{WB}}^{\boldsymbol{P}}] \end{bmatrix}^{\mathrm{T}} \\
\boldsymbol{0}_{\boldsymbol{C}} = \boldsymbol{0}_{8\times 3} \quad \boldsymbol{K}_{\boldsymbol{WB}}^{\boldsymbol{P}} = \begin{bmatrix} -2k_{z1,\mathrm{P}} & 0 & 2k_{z1,\mathrm{P}} \cdot d_{1,\mathrm{P}} \\ 0 & -2k_{z1,\mathrm{P}} \cdot b_{1,\mathrm{P}}^2 & 0 \\ -2k_{z1,\mathrm{P}} & 0 & -2k_{z1,\mathrm{P}} \cdot d_{1,\mathrm{P}} \\ 0 & -2k_{z1,\mathrm{P}} \cdot b_{1,\mathrm{P}}^2 & 0 \end{bmatrix}
\end{gathered}
\tag{36}
$$

$$
\begin{gathered}
\boldsymbol{K}_{\boldsymbol{vw}}^{\boldsymbol{A1}} = \begin{bmatrix} \boldsymbol{0}_{\boldsymbol{C}} & \mathrm{diag}[\boldsymbol{K}_{\boldsymbol{WB}}^{\boldsymbol{A1}} \quad \boldsymbol{K}_{\boldsymbol{WB}}^{\boldsymbol{A1}}] \end{bmatrix}^{\mathrm{T}} \\
\boldsymbol{K}_{\boldsymbol{WB}}^{\boldsymbol{A1}} = \begin{bmatrix} -2k_{z1,\mathrm{A}_1} & 0 & 2k_{z1,\mathrm{A}_1} \cdot d_{1,\mathrm{A}_1} \\ 0 & -2k_{z1,\mathrm{A}_1} \cdot b_{1,\mathrm{A}_1}^2 & 0 \\ -2k_{z1,\mathrm{A}_1} & 0 & -2k_{z1,\mathrm{A}_1} \cdot d_{1,\mathrm{A}_1} \\ 0 & -2k_{z1,\mathrm{A}_1} \cdot b_{1,\mathrm{A}_1}^2 & 0 \end{bmatrix}
\end{gathered}
\tag{37}
$$

$$
\begin{gathered}
i \neq 1 \\
\boldsymbol{K}_{\boldsymbol{vw}}^{\boldsymbol{Ai}} = \begin{bmatrix} \boldsymbol{0}_{\boldsymbol{C}}^{\boldsymbol{A}} & \boldsymbol{K}_{\boldsymbol{WB}}^{\boldsymbol{Ai}} \end{bmatrix}^{\mathrm{T}} \\
\boldsymbol{0}_{\boldsymbol{C}}^{\boldsymbol{A}} = \boldsymbol{0}_{4\times 2} \quad \boldsymbol{K}_{\boldsymbol{WB}}^{\boldsymbol{Ai}} = \begin{bmatrix} -2k_{z1,\mathrm{A}_i} & 0 & 2k_{z1,\mathrm{A}_i} \cdot d_{1,\mathrm{A}_i} \\ 0 & -2k_{z1,\mathrm{A}_i} \cdot b_{1,\mathrm{A}_i}^2 & 0 \\ -2k_{z1,\mathrm{A}_i} & 0 & -2k_{z1,\mathrm{A}_i} \cdot d_{1,\mathrm{A}_i} \\ 0 & -2k_{z1,\mathrm{A}_i} \cdot b_{1,\mathrm{A}_i}^2 & 0 \end{bmatrix}
\end{gathered}
\tag{38}
$$

In regular trains, the $\mathbf{0}_C$ matrix turns to $\mathbf{0}_{4\times3}$ in Eq. 37 while $\boldsymbol{K}_{\boldsymbol{WB}}^{\boldsymbol{A1}}$ reduces to its first two rows and columns. Additionally, in Eq. 38 the $\mathbf{0}_C^A$ matrix turns to $\mathbf{0}_{2\times2}$ and $\boldsymbol{K}_{\boldsymbol{WB}}^{\boldsymbol{Ai}}$ is also reduced to its first two rows and columns.

$\mathbf{K}_w$ matrix is the diagonal matrix described in Eq. 39 for articulated and regular trains.

$$\mathbf{K}_w = \mathrm{diag}\left[\boldsymbol{K}_{\boldsymbol{W_1}} \quad \ldots \quad \boldsymbol{K}_{\boldsymbol{W_i}} \quad \ldots \quad \boldsymbol{K}_{\boldsymbol{W_{Nw}}}\right], \quad \boldsymbol{K}_{\boldsymbol{W_i}} = \begin{bmatrix} 2k_{z1,\mathrm{W}_i} & 0 \\ 0 & 2k_{z1,\mathrm{W}_i} \cdot b_{1,\mathrm{W}_i} \end{bmatrix} \tag{39}$$

The damping matrices ($\mathbf{C}_v$, $\mathbf{C}_{vw}$, $\mathbf{C}_w$) present the same structure as the stiffness matrices ($\mathbf{K}_v$, $\mathbf{K}_{vw}$, $\mathbf{K}_w$); hence, they are obtained by substituting $k_{z1} \to c_{z1}$ and $k_{z2} \to c_{z2}$ in the corresponding expressions.

Finally, the $\mathbf{P}_v$ and $\mathbf{P}_w$ vectors are presented in Eqs. 40 to 44.

$$\mathbf{P}_v = \mathrm{column}\left[\boldsymbol{P}_{\boldsymbol{v}}^{\boldsymbol{P}} \quad \boldsymbol{P}_{\boldsymbol{v}}^{\boldsymbol{A1}} \quad \ldots \quad \boldsymbol{P}_{\boldsymbol{v}}^{\boldsymbol{Ai}} \quad \ldots \quad \boldsymbol{P}_{\boldsymbol{v}}^{\boldsymbol{An}} \quad \boldsymbol{P}_{\boldsymbol{v}}^{\boldsymbol{P}}\right] \tag{40}$$

$$\boldsymbol{P}_{\boldsymbol{v}}^{\boldsymbol{P}} = \left[-g \cdot m_{\mathrm{P}}^{C} \quad 0 \quad 0 \quad -g \cdot m_{\mathrm{P}}^{B} \quad 0 \quad 0 \quad -g \cdot m_{\mathrm{P}}^{B} \quad 0 \quad 0\right]^{\mathrm{T}} \tag{41}$$

$$\begin{aligned} \boldsymbol{P}_{\boldsymbol{v}}^{\boldsymbol{A1}} &= \left[-g \textstyle\sum_{i=1}^{n} m_{\mathrm{A}_i}^{C} \quad 0 \quad P_{v(3)}^{A1} \quad -g \cdot m_{\mathrm{A}_1}^{B} \quad 0 \quad 0 \quad -g \cdot m_{\mathrm{A}_1}^{B} \quad 0 \quad 0\right]^{\mathrm{T}} \\ P_{v(3)}^{A1} &= M_{adic,y}^{C} - g \cdot d_S \sum_{j=2}^{n} m_{\mathrm{A}_j}^{C} \end{aligned} \tag{42}$$

$$\begin{aligned} & i \neq 1 \\ \boldsymbol{P}_{\boldsymbol{v}}^{\boldsymbol{Ai}} &= \left[0 \quad P_{v,2}^{Ai} \quad -g \cdot m_{\mathrm{A}_i}^{B} \quad 0 \quad 0\right]^{\mathrm{T}} \\ P_{v,2}^{Ai} &= \begin{cases} -g \cdot d_2 m_{\mathrm{A}_i}^{C} - g \cdot 2d_2 \sum_{j=i+1}^{n} m_{\mathrm{A}_j}^{C} & i < n \\ -M_{adic,y}^{C} - g \cdot d_S m_{\mathrm{A}_n}^{C} & i = n \end{cases} \end{aligned} \tag{43}$$

$$\mathbf{P}_w = \mathrm{column}\left[\boldsymbol{P}_{\boldsymbol{W_1}} \quad \ldots \quad \boldsymbol{P}_{\boldsymbol{W_i}} \quad \ldots \quad \boldsymbol{P}_{\boldsymbol{W_{Nw}}}\right], \quad \boldsymbol{P}_{\boldsymbol{W_i}} = \left[-g \cdot m^{Wi} \quad 0\right]^{\mathrm{T}} \tag{44}$$

For regular trains, the 6$^{\text{th}}$ and 9$^{\text{th}}$ terms of $\boldsymbol{P}_{\boldsymbol{v}}^{\boldsymbol{A1}}$ in Eq. 42 disappear as well as the 5$^{\text{th}}$ term of $\boldsymbol{P}_{\boldsymbol{v}}^{\boldsymbol{Ai}}$ in Eq. 43.

Authors' contributions

JC implemented the train-track-bridge numerical model and the MATLAB code to solve the coupled system of equations, derived the closed-form train matrix equations, conducted the numerical simulations and validations, supported data analysis and prepared the figures. EM contributed to the conceptualisation and methodology, assisted in developing and validating the MATLAB code, supervised the formulation of the coupled system of equations and the vehicle matrices, supported the data analysis, drafted the original manuscript and reviewed the final version. PG contributed to the funding acquisition, ensured methodological coherence, supported data analysis, drafted the original draft, revised the manuscript for scientific accuracy and improved the final version. MD contributed to the funding acquisition, developed the research conceptualization and methodology, assisted in the implementation of the bridge model and numerical code, performed the data analysis, drafted the original manuscript and reviewed the final version. All authors read and approved the final manuscript.

Funding
The authors acknowledge the following institutions for their financial support: Universitat Jaume I through the contract (PREDOC/2022/26) and the grant (E-2023-08); Spanish Ministry of Science and Innovation, Agencia Española de la Investigación (AEI) and FEDER EU Funds (PID2022-138674OB-C2); Regional Government of Economic Transformation, Industry, Knowledge and Universities of Andalusia (PROYEXCEL00659); and the Andalusian Scientific Computing Centre (CICA). Funded by the European Union. Views and opinion expressed are however those of the author(s) only and do not necessarily reflect those of the European Union or the Europe's Rail Joint Undertaking. Neither the European Union nor the granting authority can be held responsible for them. The project InBridge4EU (GA No. 101121765) is supported by the Europe's Rail Joint Undertaking and its members.

Data availability
The datasets used and/or analysed during the current study are available from the corresponding author on reasonable request.

Declarations

Competing interests
The authors declare that they have no known competing financial interests or personal relationships that could have appeared to influence the work reported in this paper.

Received: 17 December 2025 Revised: 2 March 2026 Accepted: 15 March 2026
Published online: 15 July 2026

References
Aela P, Powrie W, Harkness J, Jing G (2025) Discrete element modelling of railway ballast problems: an overview. Arch Computat Methods Eng 32:2149–2185. https://doi.org/10.1007/s11831-024-10203-6
Agarwal P, Pal P, Mehta P (2022) Free vibration analysis of rc box-girder bridges using fem. Sound Vib 56(2), 105–125. https://doi.org/10.32604/sv.2022.014874
Arvidsson T, Karoumi R (2014) Train–bridge interaction – a review and discussion of key model parameters. International Journal of Rail Transportation 2(3):147–186. https://doi.org/10.1080/23248378.2014.897790
Arvidsson T, Andersson A, Karoumi R (2018) Train running safety on non-ballasted bridges. Int J Rail Transp 7(1):1–22. https://doi.org/10.1080/23248378.2018.1503975
Bonifácio C, Ribeiro D, Calçada R, Delgado R (2014) Dynamic behaviour of a short span filler-beam railway bridge under high-speed traffic. In: Pombo J (ed) Proceedings of the Second International Conference on Railway Technology: Research, Development and Maintenance, Civil-Comp Press, Stirlingshire. https://doi.org/10.4203/ccp.104.79
Bornet L, Andersson A, Zwolski J, Battini J (2015) Influence of the ballasted track on the dynamic properties of a truss railway bridge. Struct Infrastruct Eng 11(6):796–803. https://doi.org/10.1080/15732479.2014.912242
Cantero D, Arvidsson T, OBrien E, Karoumi R, (2016) Train–track–bridge modelling and review of parameters. Struct Infrastruct Eng 12(9):1051–1064. https://doi.org/10.1080/15732479.2015.1076854
CEN (2017) Railway applications - Track - Track geometry quality - Part 5: Geometric quality levels. Plain line, switches and crossings (EN13848-5:2017)
CEN (2020) Railway applications - Track - Track geometry quality - Part 6: Characterisation of track geometry quality (EN 13848-6:2014+A1:2020)
CEN (2023a) Eurocode - Basis of structural and geotechnical design – Annex A.2, application for bridges (EN 1990:2023)
CEN (2023b) Eurocode 1 - Actions on structures. Part 2: Traffic loads on bridges and other civil engineering works (EN 1991-2:2024)
Chen J, Vinod J, Indraratna B, Ngo T, Liu Y (2023) Dem study on the dynamic responses of a ballasted track under moving loading. Comput Geotech 153(105):105. https://doi.org/10.1016/j.compgeo.2022.105105
Claus H, Schiehlen W (1998) Modeling and simulation of railway bogie structural vibrations. Veh Syst Dyn 29(sup1):538–552. https://doi.org/10.1080/00423119808969585
ERRI (1999) Rail bridges for speeds >200km/h. Final report (ERRI D-214/RP9)
EU-Rail (2022) Europe's rail joint undertaking (eu-rail). https://rail-research.europa.eu/. Accessed 10 Oct 2025
Ferreira G, Montenegro P, Andersson A, Henriques A, Karoumi R, Calçada R (2024) Critical analysis of the current eurocode deck acceleration limit for evaluating running safety in ballastless railway bridges. Eng Struct 312(118):127. https://doi.org/10.1016/j.engstruct.2024.118127
Frỳba L (1999) Vibration of solids and structures under moving loads, 3rd edn. Thomas Telford, Prague
Frỳba L (2004) Dynamic behaviour of bridges due to high speed trains. In: Calçada R, Delgado R, e Matos AC (eds) Bridges for High-Speed railways: Revised papers from the Workshop, Porto, Portugal, 3–4 June 2004, 1st edn. CRC Press, London, pp 1–18
Galvín P, Romero A, Moliner E, De Roeck G, Martínez-Rodrigo M (2021) On the dynamic characterisation of railway bridges through experimental testing. Eng Struct 226(111):261. https://doi.org/10.1016/j.engstruct.2020.111261
Galvín P, Romero A, Moliner E, Martínez-Rodrigo M (2018) Two fe models to analyse the dynamic response of short span simply-supported oblique high-speed railway bridges: Comparison and experimental validation. Eng Struct 167:48–64. https://doi.org/10.1016/j.engstruct.2018.03.052
Galvín P, Romero A, Solis M, Moliner E, Martínez-Rodrigo M (2025) Time–frequency analysis of railway bridges forced and free vibrations identified by wavelet transform. Vibration 8(4). https://doi.org/10.3390/vibration8040071

Goicolea-Ruigómez JM (2008) Service limit states for railway bridges in new design codes iapf and eurocodes. In: Calçada R, Delgado R, e Matos AC, Goicolea JM, Gabaldon F (eds) Track-Bridge Interaction on High-Speed Railways: Selected and revised papers from the Workshop on Track-Bridge Interaction on High-Speed Railways, Porto, Portugal, 15–16 October, 2007, 1st edn. CRC Press, London, pp 1–12
Guo W, Xia H, De Roeck G, Liu K (2012) Integral model for train-track-bridge interaction on the sesia viaduct: Dynamic simulation and critical assessment. Comput Struct 112–113:205–216. https://doi.org/10.1016/j.compstruc.2012.09.001
Guo Y, Zhao C, Markine V, Jing G, Zhai W (2020) Calibration for discrete element modelling of railway ballast: A review. Transp Geotech 23(100):341. https://doi.org/10.1016/j.trgeo.2020.100341
INTEMAC (1991) Informe de resultados y conclusiones de las actividades de inspección técnica y prueba de carga realizadas en la estructura del puente P.K. 11+184, del tramo El Emperador-Ciudad Real sobre el río Jabalón. Tech. rep
Jia W, Markine V, Guo Y (2023) Efficiency analysis and optimisation of dem for railway ballast track simulations: Multi-layer shape model of lateral resistance. Transp Geotech 40(100):977. https://doi.org/10.1016/j.trgeo.2023.100977
Johansson C, Nualláin N, Pacoste C, Andersson A (2014) A methodology for the preliminary assessment of existing railway bridges for high-speed traffic. Eng Struct 58:25–35. https://doi.org/10.1016/j.engstruct.2013.10.011
Khatibi F, Esmaeili M, Mohammadzadeh S (2017) Dem analysis of railway track lateral resistance. Soils Found 57(4):587–602. https://doi.org/10.1016/j.sandf.2017.04.001
Martínez-Rodrigo M, Lavado J, Museros P (2010) Transverse vibrations in existing railway bridges under resonant conditions: Single-track versus double-track configurations. Eng Struct 32(7):1861–1875. https://doi.org/10.1016/j.engstruct.2010.02.022
Museros P, Andersson A, Pinazo B (2024) Dynamic behaviour of bridges under critical conventional and regular trains: Review of some regulations included in en 1991–2. Proc IME F JRail Rapid Transit 238(8):977–988. https://doi.org/10.1177/09544097241245150
Nasarre J (2004) Serviceability limit states in relation to the track in railway bridges. In: Calçada R, Delgado R, e Matos AC (eds) Bridges for High-Speed Railways Revised Papers from the Workshop, Porto, Portugal, 3–4 June 2004, 1st edn. CRC Press, London, pp 211–220
Nguyen K, Goicolea J, Galbadón F (2012) Comparison of dynamic effects of high-speed traffic load on ballasted track using a simplified two-dimensional and full three-dimensional model. Proc IME F J Rail Rapid Transit 228(2):128–142. https://doi.org/10.1177/0954409712465710
Nguyen K, Velarde C, Goicolea-Ruigómez JM (2019) Analytical and simplified models for dynamic analysis of short skew bridges under moving loads. Adv Struct Eng 22(9):2076–2088. https://doi.org/10.1177/1369433219831481
Peixer M, Montenegro P, Carvalho H, Ribeiro D, Bittencourt T, Calçada R (2021) Running safety evaluation of a train moving over a high-speed railway viaduct under different track conditions. Eng Fail Anal 121(105):133. https://doi.org/10.1016/j.engfailanal.2020.105133
Rocha J, Henriques A, Calçada R (2012) Safety assessment of a short span railway bridge for high-speed traffic using simulation techniques. Eng Struct 40:141–154. https://doi.org/10.1016/j.engstruct.2012.02.024
Sánchez-Quesada JC, Moliner E, Romero A, Galvín P, Martínez-Rodrigo MD (2024) Train-track-bridge interaction effects on highly skewed girder bridges of short-to-medium spans for increasing operating speeds. Structure and Infrastructure Engineering pp 1–25. https://doi.org/10.1080/15732479.2024.2422495
Sánchez-Quesada J (2025) Modelización avanzada y efectos de interacción vehículo–vía–estructura para el análisis del comportamiento dinámico de puentes de ffcc en vía convencional y de alta velocidad. PhD thesis, Universitat Jaume I, Castellón, Spain, (In Spanish)
Saramago G, Montenegro P, Ribeiro D, Silva A, Santos S, Calçada R (2022) Experimental validation of a double-deck track-bridge system under railway traffic. Sustainability 14:5794. https://doi.org/10.3390/su14105794
Stollwitzer A, Bettinelli L, Fink J (2023) The longitudinal track-bridge interaction of ballasted track in railway bridges: Experimental determination of dynamic stiffness and damping characteristics. Eng Struct 274(115):115. https://doi.org/10.1016/j.engstruct.2022.115115
Ticona Melo L, Ribeiro D, Calçada R, Bittencourt T (2020) Validation of a vertical train–track–bridge dynamic interaction model based on limited experimental data. Struct Infrastruct Eng 16(1):181–201. https://doi.org/10.1080/15732479.2019.1605394
Xiao Y, Luo X, Liu J, Wang K (2020) Dynamic response of railway bridges under heavy-haul freight trains. Advances in Civil Engineering 2020(1):7486,904. https://doi.org/10.1155/2020/7486904
Yang Y, Yau J, Hsu L (1997) Vibration of simple beams due to trains moving at high speeds. Eng Struct 19(11):936–944. https://doi.org/10.1016/S0141-0296(97)00001-1
Zangeneh A, Svedholm C, Andersson A, Pacoste C, Karoumi R (2018) Identification of soil-structure interaction effect in a portal frame railway bridge through full-scale dynamic testing. Eng Struct 159:299–309. https://doi.org/10.1016/j.engstruct.2018.01.014
Zhang N, Xia H, Guo W, Roeck GD (2010) A vehicle-bridge linear interaction model and its validation. Int J Struct Stab Dyn 10(02):335–361. https://doi.org/10.1142/S0219455410003464

Publisher's Note